August 2000 • NREL/SR-520-28762

Subcontractor Report

Process Development and Basic Studies of Electrochemically Deposited CdTe-Based Solar Cells

Annual Technical Report, Phase I
15 May 1998–14 May 1999

V.I. Kayadanov and T.R. Ohno
Colorado School of Mines
Golden, Colorado

National Renewable Energy Laboratory

1617 Cole Boulevard
Golden, Colorado 80401-3393

NREL is a U.S. Department of Energy Laboratory
Operated by Midwest Research Institute • Battelle • Bechtel

Contract No. DE-AC36-99-GO10337

August 2000 • NREL/SR-520-28762

Process Development and Basic Studies of Electrochemically Deposited CdTe-Based Solar Cells

Annual Technical Report, Phase I 15 May 1998–14 May 1999

V.I. Kayadanov and T.R. Ohno
Colorado School of Mines
Golden, Colorado

NREL Technical Monitor: B. von Roedern

Prepared under Subcontract No. XAK-8-17619-28

National Renewable Energy Laboratory

1617 Cole Boulevard
Golden, Colorado 80401-3393

NREL is a U.S. Department of Energy Laboratory
Operated by Midwest Research Institute • Battelle • Bechtel

Contract No. DE-AC36-99-GO10337

NOTICE

Available electronically at http://www.doe.gov/bridge

Available for a processing fee to U.S. Department of Energy
and its contractors, in paper, from:

U.S. Department of Energy
Office of Scientific and Technical Information
P.O. Box 62
Oak Ridge, TN 37831-0062
phone: 865.576.8401
fax: 865.576.5728
email: reports@adonis.osti.gov

Available for sale to the public, in paper, from:

U.S. Department of Commerce
National Technical Information Service
5285 Port Royal Road
Springfield, VA 22161
phone: 800.553.6847
fax: 703.605.6900
email: orders@ntis.fedworld.gov
online ordering: http://www.ntis.gov/ordering.htm

Printed on paper containing at least 50% wastepaper, including 20% postconsumer waste

Preface

This project, “Process Development and Basic Studies of Electrochemically Deposited CdTe-Based Solar Cells”, which is performed at the Colorado School of Mines (CSM), is part of the NREL Thin-Film Partnership Program. The project addresses long-term research and development issues related to polycrystalline thin-film solar cells. Our general research approach is based on combining activities aimed at improvement of cell performance and stability with activities aimed at increasing our fundamental understanding of the properties of materials making up the cells: CdTe, CdS, multi-layer back contact, and transparent conducting oxide (TCO) front contact. We emphasize the relation between structural and electronic material properties and various processing procedures as well as the microscopic mechanisms responsible for the cell performance and its degradation.

We believe that better basic understanding of the specific influence of polycrystallinity, especially for the fine-grain materials like those making up CdTe-based cells, is now one of the most important issues we must address. We need to clarify the role of grain boundaries (GB) in the film electronic properties as well as the electronic properties of the p-n junction. It is important to study and understand the influence of the GB boundaries on the spatial distribution of impurities and electrically active defects as well as on their migration and transformation in the course of the cell long-term normal operating conditions or under stress conditions in accelerated stability tests. To fulfill these tasks one needs to develop new methods and techniques (or adjust existing ones) for material characterization as well as more sophisticated approaches to the data analysis and modeling. This report presents studies mostly relevant to the problems formulated above that were carried out at CSM at Phase I of the project according to the Statement of Work and Tasks of the Subcontract.

Section 1 presents studies of basic electronic properties of SnO_2:F thin films produced using APCVD method at CSM in cooperation with Green Development, L.L.C. Transparency and sheet resistance of the films were close to those for the commercially available materials, such as “Nippon Glass” and “Asahi”. Bulk resistivity, Hall and Seebeck (thermopower) effects were measured as well as optical properties such as transmittance, reflection, and absorption spectra. Spectrophotometer and multi-angle spectral ellipsometry was used for studies of optical properties. Modeling the reflection spectrum and ellipsometry data based on the Drude theory provided the plasma frequency and collision frequency data. Comparative studies of Hall effect, Seebeck effect and plasma frequency in the carrier concentration range of $2x10^{20}$ to $6x10^{20}$ cm^{-3} were used to determine the electron effective mass and its dependence on the electron energy. No indication of non-parabolicity was observed in the energy range of 0.25 to 0.75 eV above the conduction band edge. Therefore in our analysis of experimental data we were able to use the transport phenomena theory specified for parabolic energy spectrum and high degeneracy of the electron gas. Contribution of the GB to the total measured resistance of the films was estimated by means of comparison of the Hall and “optical” mobilities and was found negligible for the best films. Based on thermopower data and temperature dependence of mobility, as well as on the electron scattering theory, it was shown that scattering on impurity ions screened with free electrons controls mobility in the bulk material. Calculations for the mobility value based on this scattering mechanism are in good agreement with the experimental data if we account for a spatial dispersion of dielectric constant. It was also shown that compensation of the donors by the acceptor-type native defects may lead to a significant decrease in electron mobility and hence

must be avoided when processing the TCO SnO_2 films. The section is concluded with an analysis of advantages and shortcomings of various methods for electronic properties characterization.

Section 2 is devoted to the AC characterization of thin polycrystalline CdTe and CdS films on the insulating substrates, and is predominantly methodological. The major goal of these studies was to get an opportunity to separate and study independently the individual contributions of the GB and intragrain (IG) material to the total film resistance and also measure the film capacitance. Using a Hewlett Packard 4285A LCR meter and HP-VEE software, we have developed various procedures for measurements and modeling based on reasonable physical and electrical models. Measurements on thin films of CdTe prepared in different manners and CBD CdS demonstrated the effectiveness of the method. GB and IG resistances were measured in dark and light; high photoconductivity was found to be totally due to a significant decrease in the GB resistance in light. Discussion of capacitance value led to the conclusion that the doping level (space charge density) in the vicinity of the GB is high:~10^{17}-10^{18} cm^{-3}. Studies of resistance and capacitance dependencies on bias applied to the sample revealed features that should be attributed to the increase in the GB electrical charge. A procedure was developed that enables one to derive from these dependencies the density of GB electronic states. For the CdTe films we measured, it was estimated in the range of 10^{12} to 10^{13} $cm^{-2}eV^{-1}$.

Studies of cell degradation under stress conditions are presented in Section 3. They were mostly aimed at searching for manifestations of electromigration of charged impurities/defects. For these purpose stress tests were conducted under various bias conditions (negative, positive, open circuit, maximum power), at enhanced temperature, in dark and light (~1 Sun). Cells were prepared on the CdTe/CdS structures supplied by First Solar, LLC, with application of Cu/ZnTe/Au back contact at CSM. The tests revealed considerable differences in degradation rate under different biases. The degradation degree was significantly different for different cell parameters. The stress tests were also conducted with applying different biases in sequence, e.g., positive after negative, negative after open circuit, etc. In some cases a considerable recovery of the degraded parameters was observed. As a whole, results of stress testing provided evidence of a significant role of electromigration. The results are considered as preliminary and used for developing a program for further, extended and more informative studies.

A brief description of our collaboration with other institutions within the National CdTe Team framework is presented in Section 4.

Appendices present data on personnel involved in the studies, laboratory improvements, and publications.

Table of Contents

7. Appendices

List of Figures

List of Tables

1. Studies of APCVD SnO_2:F Thin Films

1.1 Introduction

Transparent conductive thin film oxides are important basic electronic materials that have numerous applications, not only as a front contact in photovoltaic modules. Most applications require high transparency in the visible spectrum. Solar cells and flat displays also require high electrical conductivity (low sheet resistance) of the films. Today, TCOs in commercial use include tin oxide, which is usually doped with fluorine or antimony (SnO_2:F, SnO_2:Sb), tin doped indium oxide (In_2O_3:Sn≡ITO), and zinc oxide, usually doped with aluminum (ZnO:Al) [1]. The properties of these materials are adequate for most current applications, but further improvements in both conductivity and transparency are desirable, particularly for solar cells and flat panel displays.

Improving TCOs is challenging because optical and electrical properties are somewhat inversely correlated - optimal performance requires a compromise between the two. Although increasing carrier concentration through extrinsic doping increases electrical conductivity, σ, it does so at the expense of decreased transparency, T, in the visible and near IR spectrum due to free carrier absorption and reflection (shift in the plasma reflection edge). In the figure of merit of TCOs that is commonly used, transparency is weighted much higher than low sheet resistance [2], hence the limit for the doping level is defined by transparency and is usually in the range of ~ 5×10^{20} to $1\times10^{21}cm^3$. The carrier concentration in commercially available TCO's often approaches this limit. It is not practical to increase carrier concentration further, even if it were chemically possible. Thus the only possible way to increase σ (decrease sheet resistance) is to improve carrier mobility, μ.

Mobility in single crystals is defined by fundamental electronic parameters, such as the effective mass of free carriers, the dominating scattering mechanism, types and density of scatterers, etc. In polycrystalline thin film materials the mobility value is also influenced by structural imperfections, such as grain boundaries, specific point defects, voids, gaps, etc. All the factors that determine mobility in TCO thin films have not been investigated thoroughly or completely understood. There are large variations in film properties reported for TCO layers made by similar processing as well as in the estimations of the theoretical limits of mobility that could be achieved by optimizing the film structure and processing procedure. This situation explains one of the major goals of our research - basic studies of SnO_2 thin films aimed at clarification of the factors that determine mobility value in real films and estimation of the theoretical limit.

A wide variety of deposition techniques have been used to deposit TCOs, such as evaporation, sputtering, spray pyrolysis, and chemical vapor deposition (CVD). In our research atmospheric pressure chemical vapor deposition (APCVD) was used to produce SnO_2 thin films. This choice was dictated by several factors:

1. CVD is considered to be one of the best techniques and is widely used for commercial applications because it is an inexpensive process in terms of the equipment costs. The reactants are available in high purity form and the dopants can be introduced easily during

the deposition. APCVD is convenient and very productive for high-scale manufacturing on large area substrates.

2. An APCVD system for deposition on glass substrates of moderate size (4"x4") became available for us due to collaboration with Green Development, LCC.
3. Several specialists at CSM and Green Development, LCC, involved in these studies had experience in APCVD deposition of various materials.

Fluorine was chosen as a dopant providing the optimal carrier concentration in tin oxide because it is known from the literature that fluorine yields higher mobility and optical transmission than the other possible dopant, antimony.

Comprehensive characterization of the films prepared with APCVD and combined analysis of the structural, compositional, optical and electronic properties provided feedback for optimization of the processing procedure and the APCVD system design.

According to the problems to be studied and general approach formulated above, this research had the following objectives:

- To establish the set of experimental methods that can provide the information we need on the film properties.
- To provide the tools necessary for the planned experimental studies.
- To revise and optimize processing conditions and improve the APCVD system design.
- To perform experimental studies and theoretical analysis of the fundamental properties of the electronic system in tin oxide thin films, such as electron energy spectrum in the conduction band and free electron scattering.
- To clarify the factors influencing sheet resistance and bulk mobility in the actual SnO_2 films and evaluate their importance in the sense of improvement of the film electrical properties.
- To develop recommendations regarding the directions of future studies.

1.2 Characterization Methods and Techniques

Film Thickness and Surface Roughness

Accurate measurements of thickness and surface roughness are very important because of the dependence of optical and electrical measurements on these parameters. In our routine measurements, we use a surface profiler (Tencor® P-10). In order to measure the sample using the profiler, a step between the substrate and the tin oxide film surface is produced by etching the tin oxide layer using a solution of 10% concentration hydrochloric acid with zinc powder. This combination produces atomic hydrogen, which attacks the stable tin oxide. The reaction is allowed to occur on the surface of the tin oxide for approximately one minute. A position of the film is masked by a suitable tape for step preparation. The reaction does not attack the underlying glass.

In addition, ellipsometry (see Sec. 1.5) provides a good estimation of thickness and roughness, which usually agrees with profiler measurements.

The Film Structure

To characterize the crystalline properties of the films, X-ray diffraction (XRD) was used (Rigaku model Ru-200 with wavelength of 0.1541 nm, 2θ range from 15^o to 60^o with 0.05^o step

sizes, and interval of two seconds). Using this equipment we were able to determine the preferred crystallographic planes for each sample and make an estimate of the grain size. The latter was estimated based on the Scherrer formula [3]: $D = \frac{0.9\lambda}{B\cos(\theta)}$, where λ is the wavelength of the diffracted beam, θ is the angle of the diffracted peak, and B is the peak broadening in radians at half its maximum intensity.

Scanning electron microscopy (SEM) and atomic force microscopy (AFM) were used for the film morphology studies. AFM provides better space resolution and can capture the grain in three dimensions so that the roughness can be estimated.

Electrical Properties

Sheet electrical resistance is one of the two most important characteristics defining the quality of TCO films; the other is the optical transmittance. Sheet resistance, R_{sh}, and bulk resistivity, ρ, were measured routinely on all the films produced, and mapped over the film area, using the four-point probe method (an Alessi Model A 4P Series Four Probe Head, Keithley 225 current source and Keithley 181 Nanovoltmeter). The distance between neighboring collinear electrode tips was s=1 mm for all spaces. Thus the area characterized with each measurement was of the size about 3 mm × 3mm, while the sample area was usually of 4"x4". To exclude edge effects, the probes were placed on the film surface not closer than 4s from its edge. For the films, the sample thickness is much lower than the probe spacing, t<<s, the sample sizes in the two other dimensions are much greater than the distance between the probes. Under these conditions, sheet resistance and bulk resistivity are calculated as $R_{sh}=(\pi/\ln 2)(V/I)=4.532(V/I)$ and $\rho=R_{sh}t$. The results of repeated measurements on the same sample were highly reproducible.

The Hall coefficient, R_H, and Hall mobility, $\mu=R_H/\rho$, were measured with a Bio Rad HL 5500 PC Hall Effect Measurement System, which is based on the van der Pauw method. Measurements were performed on the square shaped samples $1\times1cm^2$ cut from the whole 4"×4" sample. Contacts were provided by copper wires soldered with indium/tin pellets to the corners of the sample. The size of the contact spots was made as small as possible, less than 0.5 mm, to increase the accuracy of measurements which drops as the ratio of the contact area to the sample area increases.

For measuring *the Seebeck coefficient (thermopower)* in TCO thin films deposited on insulating substrates (glass), we have designed and constructed some rather simple equipment. Figure 1.1 presents the tools and the principal scheme of the measurements.

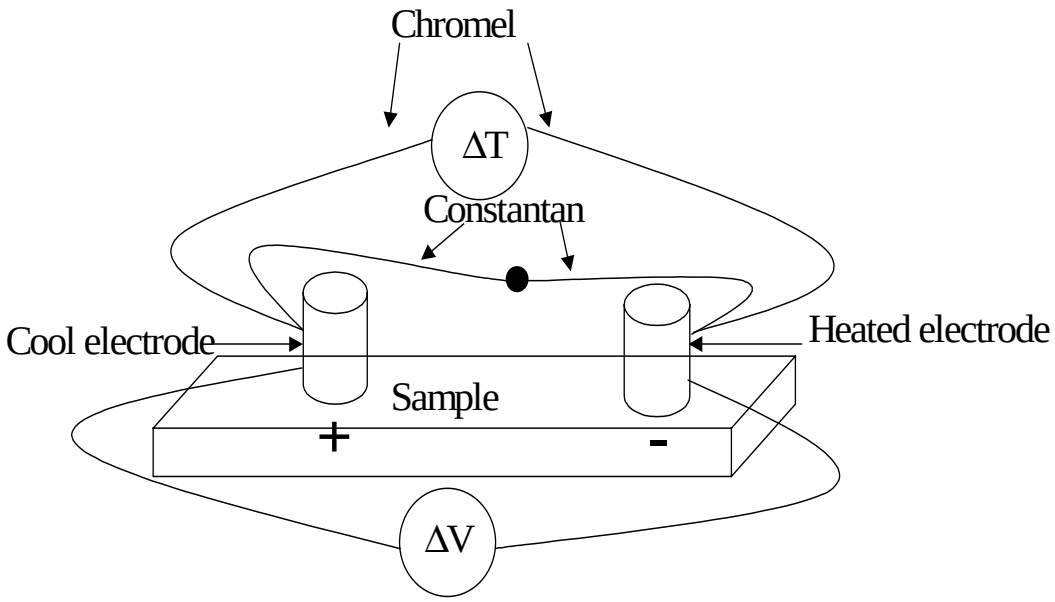

Figure 1.1 Tools for measuring Seebeck coefficient on TCO thin films

Two massive copper blocks are placed on the film surface at some distance from each other. One of the blocks is supplied with a heater, which provides heating above room temperature. The temperature of the other block is lower and does not differ significantly from room temperature because of the low thermal conductivity of glass and high heat capacitance of the block. The temperature difference between the blocks, ΔT, is measured by means of the type-E differential thermocouple and auto-ranging microvoltmeter DMM (Keithley 197A). ΔT was maintained in the range about $10^{o}C$. For the Seebeck voltage (V_S) measurement, the copper blocks were connected with copper wires to the high input resistance microvoltmeter (Keithly 192 programmable DMM). The Seebeck coefficient of the film material S_M was determined as $S_M = V_S/\Delta T + S_R$ with the reference electrode (copper) Seebeck coefficient $S_R = S_{Cu} = 2.09\ \mu V/^{o}K$ [4,5].

Massive copper blocks, due to their high weight, provided good electrical and thermal contact to the underlying film area. The latter was equipotential and isothermal. That means that we measured Seebeck coefficient of the material between the edges of the blocks. Locality of the measurements was defined by the distance between blocks and usually did not exceed 5 mm. To check how the cylindrical shape of the blocks influences the results of measurement, we performed measurements on the same films using rectangular copper blocks placed on the film surface so that the edges of the blocks were parallel to each other. No remarkable difference in the results was observed. Relocating the copper blocks on the film surface allowed us to map the Seebeck coefficient over the sample area. It was a method to check the lateral uniformity of the film properties in addition to mapping of sheet resistivity.

To verify the accuracy of the Seebeck coefficient measurements using our equipment we used foils of standard materials: constantan and nickel. Measurements at different ΔT, from 5 to $20^{o}C$, were in a good agreement with each other, and obtained values of S_M deviated less than 1% from the handbook data [6-8].

Spectrophotometry

Transmission, reflection, and absorption spectra were measured by using the Cary 5G UV-Vis-NIR spectrophotometer with a wavelength range from 250 nm to 2500 nm, which can be extended in the IR region by installing additional accessories. Both the total and diffused component of reflectance can be measured for transmission and reflection by using a different position of the sample port and an integrating sphere. The spectrophotometer consists of two incident light beams (sample and reference), an integrating sphere, and a detector. There are two sources of beams: a quartz halogen lamp for visible/IR region and a deuterium lamp for UV region. These beams have a full dimension 13×5 mm^2 and can be reduced to 9×5 mm^2. The UV-Visible detector is R298 photomultiplier tube while NIR detector is an electro-thermally controlled lead sulfide photocell.

The absorption coefficient, α, was calculated based on the transmission (T) and reflection (R) measurements, by using the relation [9, 10]:

$$T = \frac{(1+T-R)^2 e^{-\alpha t}}{(1+T)^2 - R^2 e^{-2\alpha t}}$$

The diffused component (T and R) is assumed to be very small compared with the specular component. In the wavelength region around the bandgap, where absorption is high ($\alpha t >> 1$), the absorption coefficient was also calculated by using the relation:

$$T = (1-R)^2 e^{-\alpha t}$$

Ellipsometry

A variable Angle Spectroscopic Ellipsometer (a J. A. Woollam Co. Inc. VASE© system) was used for sample characterization. Several angles of incidence (usually 65°, 70°, and 75°) and a large range of wavelengths (usually 280 nm to 1700 nm with 10 nm increments) generated a large amount of data for more accurate results.

Ellipsometry is based on measuring the change on polarization state of the reflected light from the surface of the sample. The total electric field vector can be presented by $\vec{E} = E_p \hat{p} + E_s \hat{s}$ [11], where E_p and E_s are the parallel and perpendicular (to the plane of incident) components of the electric field. Two reflectance coefficients are introduced: R_p as the ratio of the reflected E_p to the incident E_p and R_s as the ratio of the reflected E_s to the incident E_s. The ratio of these two reflectance coefficients can be expressed through two ellipsometric angles, ψ and Δ, as $\rho = \frac{R_p}{R_s} = \tan(\psi)\exp(i\Delta)$. These two measurable angles are the most commonly used in ellipsometry and usually can be determined by using what is called null ellipsometry (source - polarizer - compensator - sample - analyzer - detector).

There are various models [11, 12] that correlate these angles, Fresnel coefficient, complex dielectric constant, or index of refraction (real and imaginary parts), and the layer thickness. Designing a particular model that fits the characterization of the sample, and fitting its optical constants to the raw data obtained from ellipsometry, we can then obtain the desired information on film thickness and the optical properties of each layer in the sample. Unknown parameters in the model can be varied until the best fitting is obtained which minimizes the root mean square error (RMSE) between the created model data and the raw data.

There are several layers involved for the TCO samples characterized in this method: the glass substrate, the tin oxide layer, the rough layer on the surface and sometimes the diffusion barrier between the glass and tin oxide. In order to eliminate back surface scattering which complicates the model, the backside of the substrate was roughened using sandpaper until opaque. The TCO roughness layer was simulated using 50% of the surface material and 50% voids. Using several angles of incident beam along with a wide range of wavelengths generates a large amount of data that leads to a higher accuracy fit of the model describing the sample. Increasing the number of layers of a sample will result in complicated models.

Using a Drude model for the SnO_2 layer, the plasma frequency, ω_p and collision frequency, ω_c, can be obtained, which can be used to estimate the carrier concentration and the mobility of the sample. Since the SnO_2 layer properties can change throughout the material, a linearly graded Drude model from the bottom to the top of the layer was used in most cases. This can yield different carrier concentrations and mobilities for the top and bottom of this layer. The parameters allowed to vary in the Drude model were the thickness of the SnO_2 and roughness layers, along with ω_c, ω_p, and the complex dielectric constant, $\varepsilon=\varepsilon_1+i\varepsilon_2$ as a function of frequency. If a diffusion barrier was present, then its thickness could also vary. The optical constants of the glass substrate were determined separately and not allowed to vary. The main model used was a linearly graded Drude model, but a second slightly simpler model was also used. The second model involved only a single Drude model to which was added a linearly graded void percentage from the bottom to the top of the samples.

1.3 SnO_2 Film Growth and Properties

APCVD System and Chemistry of Deposition Process

We have grown films in a Watkins-Johnson system model 4CVD-75 for atmospheric pressure chemical vapor deposition (APCVD). It has the following features: 4 inch-wide furnace, single injector, bubblers, muffle type furnace and above 700 ^oC temperature capability. Some parts of the system were modified in the course of our research, mainly the injector design and exhaust system. The main control parameters are the reactants gas composition and flow rate, and the injector and substrate temperature. A four-inch wide continuous belt transports the substrate through the furnace. The belt speed is adjusted from 0.5 to 15 inches per minute by means of a motor controller in order to produce different thicknesses at given deposition rate. It is connected to an ultrasonic cleaner and air dryer for continuous belt cleaning.

There are three bubblers connected to the injector through heated pipes for condensation protection. $SnCl_4$ and H_2O are used as precursors, methanol as catalyst, and Freon (Difluoroethane) as a doping source. These materials react at the heated substrate producing SnO_2:F thin films:

$$SnCl_4 + n_1\,H_2O + n_2\,CH_3OH + n_3\,HF \rightarrow$$
$$SnO_2{:}F + 4\,HCl + n_4\,H2O + n_5\,CH_3OH + n_6\,HF$$

where CH_3OH is introduced to moderate the reaction by generating oxygen vacancies, and n_1 to n_6 are numerical coefficients that balance the reaction.

The source materials are in the liquid phase in reservoirs. The vapor pressure of the liquid chemical sources was carefully controlled by immersion of the bubbler vessels inside oil-filled cans. Heating the liquid leads to evaporation and dry nitrogen is then used as a carrier for the chemical vapors. The reservoir temperature, the nitrogen mass flow sensors, and the pipe temperatures control the amount of reactant chemicals. Additional nitrogen lines are added downstream from the reservoir outlets so that total gas flow into the injector can be varied without affecting the chemical composition or flow. After numerous experiments the optimal temperatures for the SnO_2 deposition were established which are presented in Table 1.1.

Table 1.1. Optimized temperatures for SnO_2:F deposition.

Substrate	550 - 600^oC
Injector	180 - 240^oC
H_2O Bubbler	80 - 90^oC
CH_3OH Bubbler	50 - 60^oC
CH_3OH/H_2O Line	100^oC
$SnCl_4$ Line	75^oC
$SnCl_4$ Bubbler	57 - 70^oC

The products of the reaction and any unreacted gases are removed with a negative pressure exhaust system. The exhaust system pulls these gases, mainly hydrochloric acid, and transports them into a fume scrubber. An excess exhaust flow reduces the deposition rate and produces turbulence of gas flow patterns leading to poor reproducibility of the deposited films. Exhaust flow was optimized based on computational fluid mechanics modeling performed by C. Wolden [13].

To avoid the non-uniform distribution of temperature across the belt, aluminum oxide ceramic plates, which have high thermal conductivity, were used to carry the substrate and provide better temperature uniformity all over the glass substrate. Large area uniform (5%) tin oxide thin films (t~400-500 nm) in a large-scale production can now be deposited reproducibly with the desired properties of the material.

Film Properties

A typical image of a SnO_2:F film of a thickness of about 450 nm is presented in Fig. 1.2 The average grain size determined with AFM and SEM for many films was in a range from 130 to 200 nm. We did not notice any relation between the thickness and the grain size for thickness between 350 to 850 nm. XRD revealed peaks corresponding to (211), (101), (200), and (110) planes with d-space of 1.7735±0.0022, 2.6612±0.0027, 2.376±0.0036, and 3.3723±0.0027 Å respectively, which is in a good agreement with the data on d-space for SnO_2 powder for the same planes: 1.765, 2.644, 2.369, and 3.351 Å [14]. Typically no significant differences in the peak intensities were observed, hence no conclusions on the preferential orientation could be made.

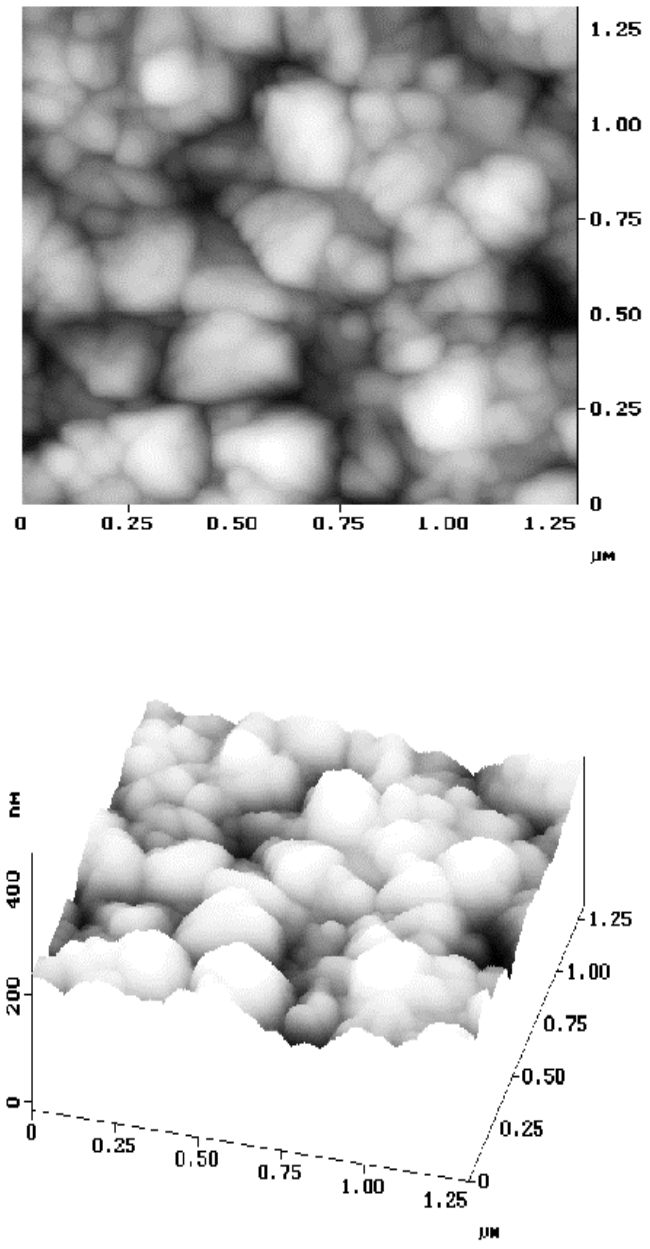

Figure 1.2 AFM image of SnO_2 thin film on Soda Lime glass substrate.

Table 1.2 presents the main optical and electrical characteristics of some of the deposited films compared with the properties of commercial tin oxide films measured using the same characterization equipment

Table 1.2 Comparison of commercial SnO_2 films and those deposited at CSM by APCVD. Transparency and haze are averaged over the wavelength range of 500 to 900 nm.

Sample	Substrate	Thickness nm	Sheet Resistance Ω / □	Mobility cm^2/Vs	Carrier Concentr. $10^{20}\ cm^{-3}$	Transparency %
Nippon	Soda Lime/SiO_2	500	9.5	29.0	4.5	80.5
CSM	Soda Lime	370	12.0	25.0	5.6	80.3
CSM	Soda Lime	330	14.0	26.0	5.2	82.0
Asahi	Soda Lime/SiO_2	800	13.5	34.0	1.8	79.0
CSM	Soda Lime	690	11.2	29.0	2.9	79.0
CSM	Soda Lime	610	13.4	29.0	2.6	82.0

In general, our samples have carrier concentration of $1 \times 10^{20} – 6 \times 10^{20}$ /cm^3, and mobility from 14 to 30 cm^2/V.s. Spectrophotometer measurements showed that the optical transmission of our samples in the spectral range of 500-900 nm is around 80% with average reflectance of ~ 10%. The optical absorption coefficient, α, of our tin oxide films is very small in this spectral range. The bandgap value derived from the graphs of photon energy, E_{ph}, versus $(\alpha E_{ph})^2$ in a high energy region, varied for different films in the range from 3.95 eV to 4.25 eV. We did not analyze possible reasons for the variation. The reflectance plasma edge is well pronounced in the low energy region and shifts toward shorter wavelength as carrier concentration increases in agreement with Drude model (see Sec. 1.4).

1.4 Basic Electronic Properties of SnO_2:F Thin Films

This section presents studies of SnO_2 thin films aimed at determination and discussion of the fundamental parameters of the electron system in this material which are relevant to one of the most important characteristics of TCOs, i.e., carrier mobility. Our approach is based on experimental studies and combined analysis of a variety of transport phenomena including AC conductivity in a high frequency (optical) range. We will start this section with the theoretical basis of our studies, then present and discuss the results of experiments.

1.4.1 Approximations of the Theory and Verification of Their Validity.

The equations that relate the measured characteristics of a material to the fundamental parameters, such as carrier concentration, mobility, effective mass, collision time, mean free path length, and dominating scattering mechanism, are presented in many publications and textbooks [15, 16]. They were derived based on some simplifications and approximations of the general theory. Before using these equations we analyzed the validity of these assumptions and

approximations with respect to the specific properties of the heavily doped SnO_2 thin films known from literature and our own studies presented in this report.

Quasi-Continuous Electron Spectrum

When the film thickness is very small, one has to discuss a possible influence of the quantum-size effect. The electron spectrum will be quantized if the electron de Broglie wavelength, λ_e, is comparable to the film thickness. The electron gas in our heavily-doped material (carrier concentration ranged from 1×10^{20} to 6×10^{20} cm^{-3}) is highly degenerate. Hence only those electronic states contribute to the transport phenomena whose energy is close to the Fermi level, that is whose wave vector **K** is close to the Fermi surface in the **K**-space. Corresponding λ_{eF} values, can be estimated using the formulae: $\lambda_{eF}=2\pi/K_F=2\pi/(3\pi^2 n)^{1/3}$. For the concentrations mentioned above, that gives values of in the range of 25 to 43 Å. The typical thickness of the films studied was in the range of thousands of Angstroms. Thus quantum-size effect can be neglected and the spectrum can be considered as continuous.

Quasi-Classical Approximation

In this approximation the electrons are treated as particles with simultaneously well-defined space coordinates and momentum/velocity values, and hence the Boltzmann equation formalism can be used. Good agreement of theory to the published experimental results has been reported for many other semiconductor materials with fundamental characteristics similar to those of SnO_2, such as carrier concentration and mobility, effective mass, etc. In particular, Si, some III-V semiconductors, PbTe, and PbSe, can be mentioned.

Relaxation Time Approximation

Electric and heat currents are zero in equilibrium when the distribution of electrons over the band states is described by the Fermi-Dirac function:

$$f_0=\{1+\exp[(E-E_F)/k_BT]\}^{-1} \qquad (1.1)$$

where E_F is Fermi level and k_B is the Boltzmann constant.
External fields perturb the distribution from equilibrium while scattering processes drive the distribution to equilibrium. A stationary non-equilibrium distribution f(**K**) is formed under the action of these two factors. To define the non-equilibrium f(**K**) the Boltzmann equation can be used which in general is an integro-differential one. The mathematical problem is simplified significantly if the collision integral, I_{col}, which represents the scattering processes in the equation, can be reduced to a simple analytical form:

$$I_{col} \equiv \left[\frac{\partial f(\mathbf{K})}{\partial t}\right]_{col} = -\frac{[f(\mathbf{K}) - f_o]}{\tau(\mathbf{K})} \qquad (1.2)$$

This means that after the external fields have been switched off, the non-equilibrium distribution is relaxing according to the equation:

$$f(\mathbf{K}, t)-f_o= [f(\mathbf{K}, 0) - f_o(\mathbf{K})]\exp(-t/\tau).$$

The parameter τ is called the relaxation time and defines the rate of the equilibrium restoration.

The relaxation-time approximation is especially justified when scattering processes are elastic, that is if the change in the electron energy due to the collision is much smaller than the

initial energy. That is the case for scattering by impurities, point defects, dislocations, and grain boundaries. For the phonon scattering, relaxation time approximation is always valid if the Fermi energy is much higher than the characteristic phonon energies. That is the case for our materials where Fermi energy ranges from 0.25 to 0.75 eV (see Sec.1.4.3) and the maximum phonon energies are lower by an order of magnitude.

Isotropic Electron Spectrum

Analysis of electron transport is rather complicated if the constant energy surfaces in **K**-space are non-spherical. In this case the effective mass must be in general treated as a tensor that varies from one point in the **K**-space to another. Relaxation time also depends on the **K** magnitude and direction but can be treated as a tensor for some special cases. For the isotropic spectrum, both m* and τ are scalars and their magnitudes depend only on the magnitude of **K**, that is only on the carrier energy. According to Ref. 17, the constant energy surfaces in SnO_2 are represented by ellipsoids of revolution with slightly different (about 10%) lengths of the ellipsoid axes. This very small difference enables us to use the isotropic approximation for SnO_2 without significant errors in calculated transport coefficients. There are two more reasons to make this assumption: (a) among the transport coefficients we have studied only electrical conductivity/mobility is anisotropic, but the estimate of this anisotropy based on Ref. 18 does not exceed 20-25 %; the Hall and Seebeck coefficients are isotropic for the ellipsoidal constant energy surfaces; (b) our films do not have some well defined crystallographic orientation, hence even the conductivity should be averaged over the directions of the grain orientation and be macroscopically isotropic. Thus we assume that E(**K**)=E(K).

Parabolic Electron Spectrum

E(**K**) dependence in general can be approximated by a parabola only in the vicinity of the band extremum, that is close to the band edge. As K value increases, the E dependence on K becomes slower than K^2. The higher the energy of carriers, the greater the influence of non-parabolicity. For many direct-gap and narrow-gap semiconductors such as InSb, GaSb, PbSe, $Hg_{1-x}Cd_xTe$, and $Pb_{1-x}Sn_xTe$, non-parabolicity was studied in detail both theoretically and experimentally (the latter in heavily doped materials or at elevated temperatures) and found well pronounced and important for transport phenomena (e.g. see [15,16]). One of the most prominent manifestations of the non-parabolicity is the growth of effective mass with Fermi level. For SnO_2 there were a few attempts to investigate non-parabolicity, but published data are controversial, see, e.g., [19] and [20]. We have studied experimentally the effective mass dependence on the Fermi level position in a wide range of the latter (from 0.25 to 0.75 eV) by means of comparison of the measured Hall and Seebeck coefficients and plasma frequency (see Sec.1.4.3). We did not find any indication of effective mass growth with carrier concentration (Fermi level) increase. Therefore we assume parabolic spectrum for materials we studied.

High Degeneracy of the Carrier Gas and Sommerfeld Approximation

With all the approximations discussed above, the theory comes to the following equations for electrical conductivity, the Hall and Seebeck coefficients in the n-type semiconductor:

$$\sigma = \frac{nq^2}{m^*}\langle\tau\rangle; R_H = -\frac{1}{qn}\frac{<\tau^2>}{<\tau>^2}; \quad S = -\frac{1}{qT}\frac{<(E-\eta)\tau>}{<\tau>} \qquad (1.3)$$

where $\eta=E_F-E_C$ is the Fermi level position with respect to the conduction band edge; <...> symbolizes averaging of a function of E over all the energy band states with a weight function $W=(-\partial f_o/\partial E)\cdot D(E)\cdot v(E)^2$, where $D(E)=[4\pi\cdot(2m^*)^{3/2}/h^3]\cdot E^{1/2}$ and $v=(2E/m^*)^{1/2}$ are the density of states function and electron velocity, respectively, and h is the Planck constant.

The distribution function f_o, as well as $(-\partial f_o/\partial E)$, drop to zero exponentially for $(E-E_F)/k_BT>1$, hence the finite extent of a band is well simulated by the limit $E=\infty$ when integrating over the band spectrum. The lower band edge will be taken as an origin of energy scale ($E_{min}=0$). Thus the averaging of some function $\Theta(E)$ is described by the equation:

$$\langle\Theta(E)\rangle=\frac{\int_0^\infty \Theta(E)E^{3/2}\left(-\frac{\partial f_o}{\partial E}\right)dE}{\int_0^\infty E^{3/2}\left(-\frac{\partial f_o}{\partial E}\right)dE} \qquad (1.4)$$

The function $(-\partial f_o/\partial E)$ drops exponentially to zero on both sides of $E=E_F$. Indeed,

$$\left(-\frac{\partial f_o}{\partial E}\right)=\frac{1}{4k_BT\cosh^2[(E-\eta)/2kT]}$$

Hence, in the case of high degeneracy, $\eta/k_BT>>1$, only the states with the energy close to the Fermi level contribute considerably to the integrals above. In addition,

$$\int_{-\infty}^{\infty}\left(-\frac{\partial f_o}{\partial E}\right)dE=f_o(-\infty)-f_o(+\infty)=1-0=1$$

Thus the properties of $(-\partial f_o/\partial E)$ function are similar to those of the δ-function if one takes into account that, due to the rapid converging of the integral, replacement of 0 as a lower limit by $-\infty$ does not change the integral value. The so-called Sommerfeld approximation is commonly used for calculation of the integrals like those in Eq. 1.4, in the case of high degeneracy:

$$\int\Phi(E)\left(-\frac{\partial f_o}{\partial E}\right)dE\approx\Phi\Big|_{E=\eta}+\frac{\pi^2}{6}\frac{\partial^2\Phi}{\partial E^2}\Big|_{E=\eta}(k_BT)^2 \qquad (1.5)$$

This approximation is valid under conditions: (a) $\eta/k_BT>>1$ (high degeneracy); (b) magnitude of $\Phi(E)$ does not change considerably within the energy interval $\sim k_BT$ where $\left(-\frac{\partial f_o}{\partial E}\right)$ is essentially non-zero; (c) $\Phi(E)$ is smooth in this energy interval, that is $[\Phi^{-n}(\partial^n\Phi/\partial E^n]_{E=\eta}(k_BT)^n<<1$. If all these conditions are satisfied, we have to the first non-vanishing approximation:

$$\int\Phi(E)\left(-\frac{\partial f_o}{\partial E}\right)dE\approx\Phi\Big|_{E=\eta} \qquad (1.6)$$

If $\Phi(E)=(E-\eta)\cdot\Psi(E)$, then $\Phi\big|_{E=\eta}=0$ and we can not neglect the second term in Eq. 1.5. In this case one obtains the first non-vanishing approximation:

$$\int \psi(E)\left(-\frac{\partial f_o}{\partial E}\right)(E-\eta)dE = \frac{\pi^2}{3}\frac{\partial \Psi}{\partial E}\Big|_{E=\eta}(k_B T)^2 \qquad (1.7)$$

For Φ being a power function of energy: $\Phi(E)=E^P$, one obtains from Eq. 1.5:

$$\int E^P\left(-\frac{\partial f_o}{\partial E}\right)dE \approx \eta^P\left(1+\frac{\pi^2}{6}P(P-1)(k_B T/\eta)^2\right)$$

When the averaged function $\Theta(E)=E^S$ (see Eq.1.4), one obtains:

$$<E^S>=\eta^S[1+(\pi^2/6)S(S+2)(k_B T/\eta)^2] \qquad (1.8)$$

In the next section some numerical estimates of possible inaccuracy in calculating transport coefficients based on the Sommerfeld approximation will be presented.

1.4.2 Equations for Transport Coefficients and Their Analysis

Transport coefficients for the stationary external fields

To calculate σ, R_H, and S (see Eqs. 1.3), one needs to know the energy dependence of relaxation time, τ. Assuming that $\tau(E)$ is a smooth function in the vicinity of Fermi level, we will approximate it in this region with a power function:

$$\tau(E) = \tau(\eta)(E/\eta)^r \qquad \text{where } r \equiv d\ln\tau / d\ln E\Big|_{E=\eta} \qquad (1.9)$$

The parameter r value depends on the dominating scattering mechanism and usually is referred to as the "scattering parameter".

Now, based on the Sommerfeld approximation and Eqs. 1.8 and 1.9, one obtains

$$\langle\tau\rangle = \tau(\eta)\left[1+\frac{\pi^2}{6}r(r+2)(k_B T/\eta)^2\right] \qquad (1.10)$$

$$\frac{\langle\tau^2\rangle}{\langle\tau\rangle^2} = 1+\frac{\pi^2}{3}r^2(k_B T/\eta)^2 \qquad (1.11)$$

$$\frac{\langle(E-\eta)\tau\rangle}{\langle\tau\rangle} = \frac{\pi^2}{3}\left(r+\frac{3}{2}\right)\frac{(k_B T)^2}{\eta} \qquad (1.12)$$

According to our estimates, the lowest Fermi level value for the materials we studied is $\eta\approx 0.25$ eV which corresponds to $n=1\times10^{20}$ cm^{-3}. At room temperature (T=300 K), $k_BT=0.0258$ eV, hence the small parameter, $(k_BT/\eta)^2$, value does not exceed 0.0105. Our analysis of the measured Seebeck coefficient showed that the scattering parameter value is not greater than 1($r\le1$). Thus, neglecting the second term in square brackets in Eq. 1.10 leads to an error not greater than 5%. For the films with $n=5\times10^{20}$cm^{-3} the estimated inaccuracy is lower by an order of magnitude. Even smaller inaccuracy comes from neglecting the second term in the right side of Eq. 1.11. We have compared the $\frac{\langle(E-\eta)\tau\rangle}{\langle\tau\rangle}$ values calculated based on Eq.1.12 (Sommerfeld

approximation) with those obtained by using the exact equation for arbitrary degeneracy, which includes the Fermi integrals. The difference between the two does not exceed 3% for $\eta/k_BT \geq 10$.

Thus, with sufficient precision we can use the Sommerfeld approximation and describe transport coefficients with rather simple equations:

$$\sigma = (nq^2 / m^*)\tau(\eta) \tag{1.13}$$

$$R_H = -(qn)^{-1} \tag{1.14}$$

$$S = -(k_B / q)(\pi^2 / 3)(r + 3/2)(k_B T / \eta) \tag{1.15}$$

For the parabolic and isotropic model in the Sommerfeld approximation, carrier concentration is defined by

$$n = \frac{8\pi(2m^*)^{3/2}}{3h^3}\eta^{3/2}\left[1 + \frac{\pi^2}{8}\left(\frac{k_B T}{\eta}\right)^2\right] \tag{1.16}$$

The correction term in the square brackets is less than 1.3% for $\eta / k_BT \geq 10$, thus we can use the simplified formulas:

$$n = \frac{8\pi(2m^*)^{3/2}}{3h^3}\eta^{3/2} \tag{1.17}$$

and

$$\eta = \left(\frac{3}{8\pi}\right)^{2/3} \frac{h^2}{2m^*} n^{2/3} \tag{1.18}$$

Substituting the last expression for η in Eq. 1.15, we obtain a useful equation that relates the Seebeck coefficient to the carrier concentration, effective mass, scattering parameter r and temperature:

$$S = -27.2(k_B/q)\frac{(r + 3/2)m^*}{h^2}(k_B T)n^{-2/3} \tag{1.19}$$

Now let us summarize the results presented above with respect to what information on the fundamental parameters of material can be obtained from the measurements of electrical conductivity, the Hall and Seebeck coefficients. Hall effect measurements provide the carrier concentration value:

$$n = -(qR_H)^{-1} \tag{1.20}$$

Combination of conductivity or resistivity, σ or ρ, and the Hall coefficient, R_H, gives a mobility, μ, value:

$$\mu = |R_H|\sigma \qquad \text{or} \qquad \mu = |R_H| / \rho \tag{1.21}$$

Based on Eq. 1.13, mobility can be defined as

$$\mu = \sigma / qn = q\tau(\eta) / m^* \tag{1.22}$$

Mean free path length of a carrier, *l*, is the product of a mean free path time (relaxation time), τ, and the carrier velocity, v: $l=\tau v= l(\eta) = \mu m * v(\eta) / q = \mu P(\eta) / q$,
where P(η) is a momentum value for the electron with the energy equal to the Fermi energy. It can be easily calculated from the known carrier concentration using the formula: $P(\eta) = (3/8\pi)^{1/3} hn^{1/3}$. Thus the mean free path length can be determined from measurements of R_H and σ by using either of the two equations below:

$$l(\eta) = (3/8\pi)^{1/3} h\mu n^{1/3} / q \qquad (1.23)$$

$$l(\eta) = (3/8\pi)^{1/3} h\sigma \left|R_H\right|^{2/3} / q^{4/3} \qquad (1.24)$$

The expression for the Seebeck coefficient (Eq.1.19) contains three fundamental parameters of a material: effective mass, m*, scattering parameter, r, and carrier concentration, n. If two are known, the third one can be determined from S measurement. In our study we used this equation to derive the scattering parameter which is a signature of the dominating scattering mechanism. Carrier concentration was determined by Hall measurements, and effective mass value was determined from comparison of the Hall and plasma frequency measurements.

AC Electrical Conductivity (Plasma and Collision Frequencies)

In this section we will consider the electrical current induced by a time-dependent (non-stationary) electric field. We will base our analysis on the approximations discussed in Sec. 1.4.1 and shown to be valid for the heavily doped SnO_2. Briefly, we assume the electron spectrum is continuous and isotropic; dissipation of momentum occurs due to scattering of electrons by defects or phonons; scattering processes can be treated in the relaxation time approximation; and the electron gas is degenerate. The latter means that only electrons with energy close to the Fermi energy contribute to electrical transport, and hence dynamic properties (effective mass, m*) and collision time, τ, or collision frequency, $\omega_c=1/\tau$, are the same for all those electrons. These approximations enable us to use the Drude model, which is commonly applied to the AC conductivity and optical properties analysis in metals.

AC conductivity is a complex value and depends on the frequency of the electric field

$$\sigma(\omega) = \frac{\sigma_0}{1 - i\omega\tau} = \frac{q^2 n\tau}{m^*} \frac{1}{1 - i\omega\tau} \qquad (1.25)$$

High electrical conductivity in metals and heavily doped semiconductors, and its dependence on frequency, significantly influences optical properties of these materials, in particular the transparency and reflectivity spectra. The wave equation contains a complex dielectric constant with the real and imaginary parts presented by:

$$\mathrm{Re}\,\varepsilon = \varepsilon' = n^2 - k^2 = \varepsilon_\infty \left(1 - \frac{\omega_p^2}{\omega^2 + \omega_c^2}\right); \qquad \mathrm{Im}\,\varepsilon = \varepsilon'' = 2nk = \varepsilon_\infty \left(\frac{\omega_p^2 \omega_c}{\omega(\omega^2 + \omega_c^2)}\right)$$

Here *n* and *k* are refractive index and extinction coefficient respectively, and ε_∞ is the "high-frequency" dielectric constant for which the bound electrons are responsible. The equations include two characteristic parameters that are totally defined by free (conductive) electrons. Those are the collision frequency, $\omega_c=1/\tau$, and the plasma frequency, ω_p, which is a natural frequency of oscillations of the electron gas as a whole. The latter is given by equation

$\omega_p=[4\pi q^2 n/(m^*\varepsilon_\infty)]^{1/2}$.

When the frequency of an electromagnetic wave comes close to the plasma frequency, then reflectivity and transparency of the material can change dramatically. If $\omega_c<<\omega_p$, then to a first approximation $\varepsilon \approx \varepsilon' = \varepsilon_\infty (1-\omega_p^2/\omega^2)$. For real and negative ε ($\omega<\omega_p$), the solutions to the wave equation decay exponentially in material; i.e. no radiation can propagate. When ε is positive ($\omega > \omega_p$), solutions become oscillatory, and the conductor should become transparent. Thus at $\omega=\omega_p$ there should be observed a sharp change in reflectivity which is known as "plasma reflectivity edge" and also in transparency. For real conductors, ω_c/ω_p is usually not so small, therefore reflectance does not change so sharply when frequency crosses the ω_p value. Analysis of the measured optical spectra allows us to determine plasma and collision frequencies. That provides an independent method for measurement of carrier concentration and mobility if the effective mass is known. Indeed,

$$n=\omega_p^2 m^*\varepsilon_\infty/4\pi q^2 \qquad (1.26)$$

As to mobility, it can be calculated based on the measured value of $\omega_c=1/\tau$ and equation (1.22) so that

$$\mu=(q/m^*)/\omega_c \qquad (1.27)$$

1.4.3 Experimental Results and Discussion

Plasma Frequency and Seebeck Coefficients vs. Hall Concentration. Effective mass.

The objective of studies presented in this section is to determine the effective mass value and its dependence (or independence) on the carrier concentration. The effective mass knowledge is important for further analysis of mobility and scattering mechanisms. As to the m*(n) dependence, it is an indicator of whether the formulas presented in Sec. 1.4.2 could be applied to this analysis. The effective mass that appears in the equations for the transport coefficients and Fermi level-concentration relation, is defined by the equation

$$\frac{1}{m^*} \equiv \frac{1}{P}\frac{dE}{dP} \qquad (1.28)$$

where $P = \hbar K$ is the electron momentum. To analyze the influence of non-parabolicity it is convenient to present the E(P) dependence in the form:

$$P^2/2m_0^*=E[1+\Gamma(E)] \qquad (1.29)$$

where m_0^* is the limiting value of the effective mass when energy drops to zero. Within the energy range, where the contribution of Γ can be neglected (parabolic spectrum), the effective mass is constant and equal to m_o^*, the density of states function is $D(E)=4\pi(2m_o^*/h^2)^{3/2}E^{1/2}$, and the carrier concentration at high degeneracy is defined by $n=(8\pi/3)(2m_o^*/h^2)^{3/2}\eta^{3/2}$. In the range of higher energies, where Γ value is not negligible, one has:

$$m^* = m_o^*\left[1+\Gamma(E)+E d\Gamma/dE\right] \qquad (1.30)$$

$$D(E) = 4\pi(2m_o^*/h^2)^{3/2}E^{1/2}\left[1+\Gamma(E)+E d\Gamma/dE\right] \qquad (1.31)$$

$$n = (8\pi/3)(2m_o^*/h^2)^{3/2}\eta^{3/2}[1+\Gamma(\eta)]^{3/2} \qquad (1.32)$$

Since $\Gamma(E)>0$ and $d\Gamma/dE>0$, the effective mass value increases with energy, density of states increases with energy more rapidly than in the parabolic case, as well as the carrier concentration does with the Fermi level. Conversely, the Fermi level increases with carrier concentration slower than in the parabolic case.

Let us now consider how non-parabolicity influences the expressions for the transport coefficients presented and discussed in Sec. 1.4.2. As long as the electron gas is highly degenerate ($\eta/k_BT>>1$), the expressions obtained in the Sommerfeld approximation (Eq. 1.5) by neglecting the term $\propto (k_BT/\eta)^2$, such as those for R, μ, and ω_p, preserve their form although now effective mass is a function of the Fermi level position, that is of concentration:

$$R_H = -(qn)^{-1}, \qquad \mu = \sigma/qn = q\tau(\eta)/m^*(\eta), \qquad \omega_p = \sqrt{\frac{4\pi nq^2}{m^*(\eta)\varepsilon_\infty}}.$$

At the same time an inaccuracy of these expressions due to neglecting the term $\propto (k_BT/\eta)^2$ can increase. In contrast, for the Seebeck coefficient it is essential to preserve the second term in the Sommerfeld approximation. The new equation for the Seebeck coefficient contains $\Gamma(E)$, $d\Gamma/dE$, and $d^2\Gamma/dE^2$ terms calculated at $E=\eta$. Thus, to analyze the Seebeck coefficient we need first determine the $\Gamma(E)$ function.

We did that by means of measuring and comparing Hall concentration and ω_p values on the set of the SnO_2 films with different doping levels. As the carrier concentration increases, the Fermi level also increases, no matter whether the band is parabolic or not. The Hall concentration varied in a range of 1.8×10^{20} to 5.6×10^{20} cm^{-3}, which provided considerable variation in the Fermi level position. Because of the high n value and also based on thermopower measurements, one could conclude that the electron gas in all the samples is highly degenerate.

Figure1.3. presents m*(n). Plasma frequency was measured by both spectrophotometry and ellipsometry measurements. Effective mass was calculated by using Eq. 1.26 with $\varepsilon_\infty=4$ derived from our ellipsometry measurements, which is very close to the literature data. It is seen that within the spread of the experimental points the m* value is constant, which means that no considerable deviation from parabolicity takes place for our material in the carrier concentration range indicated above (and also in corresponding range of the electron energies). This is a very important result, which enables us to use the simple parabolic band theory in further analysis of the experimental data.

The effective mass value determined is $m^*=(0.28\pm0.03)m_o$. According to [17], the longitudinal and transverse effective mass components (that is parallel and perpendicular to the revolution axis of the ellipsoidal constant energy surface) are: $m_\parallel^*=0.234m_0$ and $m_\perp^*=0.299m_0$. When averaged over all directions, that provides the value of the "effective mass of conductivity", m_c^*, which defines the plasma frequency and mobility for the ellipsoidal constant energy surface: $1/m_c^*=1/3[(1/m_\parallel^*)+(1/m_\perp^*)]$. The result of calculation is: $m_c^*=0.274m_0^*$. It should be noted, that for the ellipsoidal constant energy surface the so called "density of states effective mass", m_d^*, is defined as $m_d^*= (m_\parallel^* m_\perp^{*2})^{1/3}$. This mass is included in the expressions for density of states, carrier concentration and Seebeck coefficient. Calculated for the same effective mass components, $m_d^*=0.276m_0$. Thus, m_d^* and m_c^* values coincide with each other

closely and with our experimental m* value. This verifies the isotropic spectrum approximation that we will use. We assume the effective mass value to be $0.275m_o$*.

An independent confirmation of the parabolicity comes from the Seebeck coefficient dependence on carrier concentration. The Seebeck coefficient, S, is proportional to $n^{-2/3}$ for parabolic band in the case of high degeneracy. For the non-parabolic band S(n) dependence changes and becomes more complicated. As seen from Fig. 1.4., the experimental dependence S(n) obtained by us is very close to $n^{-2/3}$. Using Eq. 1.19 and the effective mass value indicated above we calculated the scattering parameter, r, value (see Fig.1.5). The latter will be used in Sec. 1.4.4 for identification of the scattering mechanism.

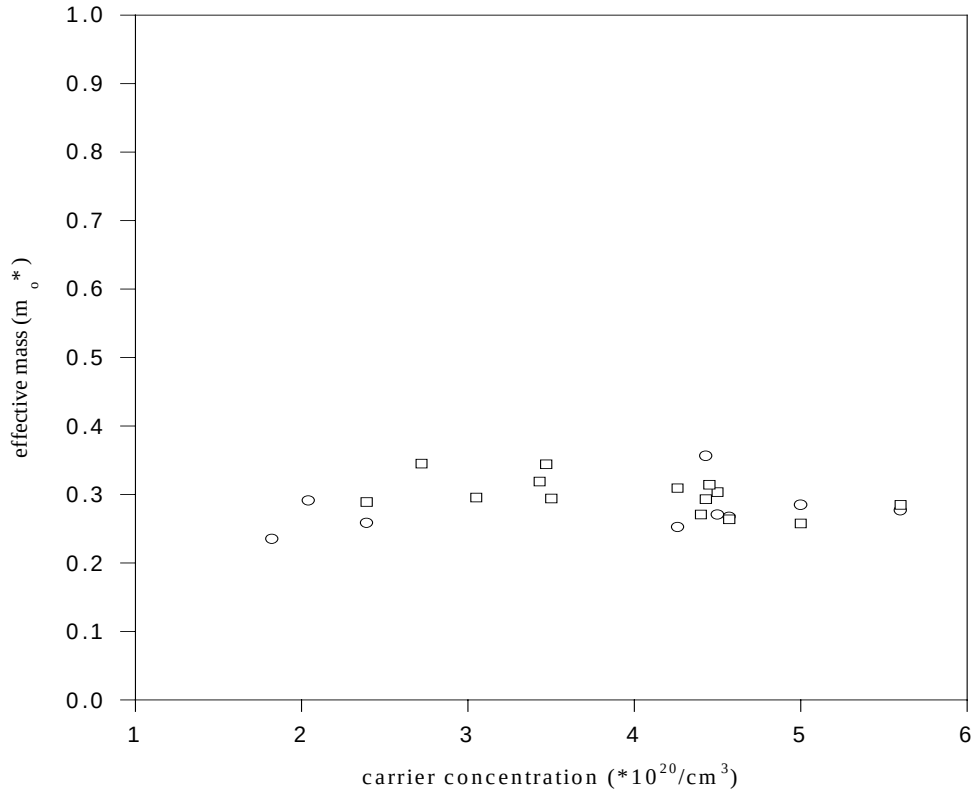

Figure 1.3 Plasma frequency from both ellipsometry (○) and reflection measurements (□) against carrier concentration for some tin oxide films.

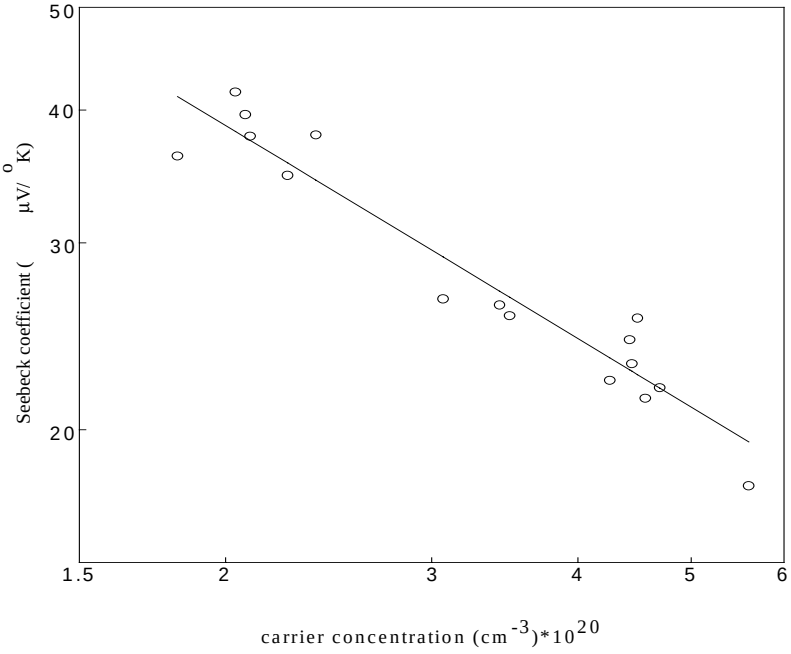

Figure 1.4 Carrier concentration vs. magnitude of the Seebeck coefficient . In the double-log. scale, the dependence is represented by the straight line with a slope corresponding to $S \propto n^{-2/3}$

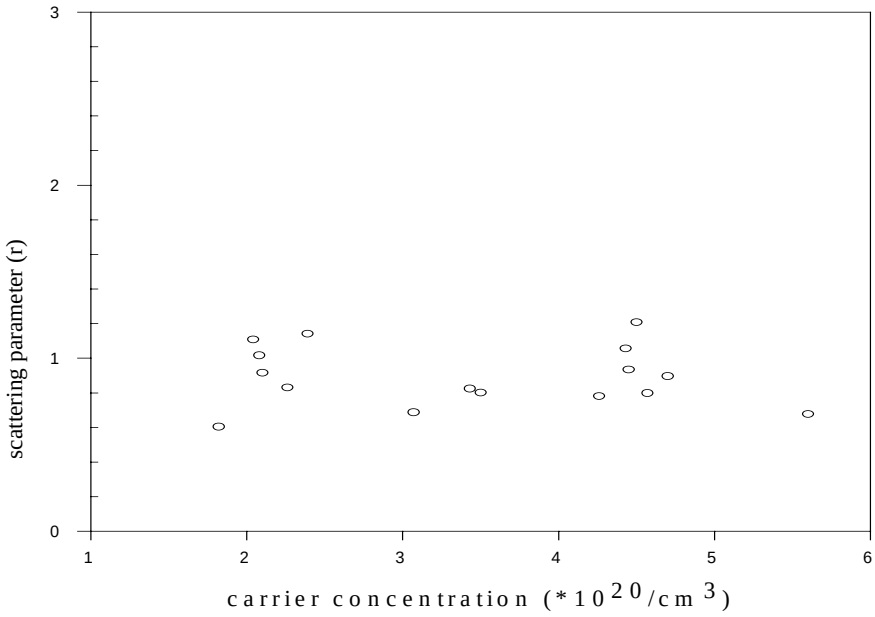

Figure 1.5 Carrier concentration vs. scattering parameter

Resistivity and Mobility (Influence of the Grain Boundaries)

A significant difference is usually observed between mobility ($\mu=[q\rho n]^{-1}$) values measured on single crystal and polycrystalline samples of the same material (the same composition, carrier concentration, etc.). For example, resistivity measured on CdS or CdTe polycrystalline films could be several orders of magnitude higher than that for single crystals. This difference is usually attributed to the influence of the grain boundaries (GB). Electronic properties of the material in the GB region may be significantly different from those in the bulk of the grains. Deep electronic levels that exist at the interface between two grains trap the majority carriers and hence acquire some electrical charge, which provides a potential barrier for the majority carriers. Thus the GB behaves like two Schottky diodes connected back-to-back.

It is common to treat the problem of the GB influence on resistance in terms of "GB-scattering". This terminology is not always correct and sometimes can be misleading. Indeed, frequency of scattering, $1/\tau$, is an important parameter that in combination with the effective mass determines the mobility value. Carriers are scattered by impurities, point defects, dislocations, by phonons (scattering in the grain bulk, or B-scattering) and also by GB (GB-scattering). For several coexisting scattering mechanisms, the total collision frequency is the sum of the partial ones:

$$1/\tau = 1/\tau_1 + 1/\tau_2 + 1/\tau_3 + ... = 1/\tau_B + 1/\tau_{GB}$$

The individual contribution of the GB scattering can be evaluated by comparison of $1/\tau_{GB}$ and total scattering frequency, $1/\tau$. For this purpose it is convenient to rewrite the previous equation in terms of mean free paths, $l_i = \tau_i v$. Velocity, v, for high degeneracy is the Fermi velocity that is the same for all the electrons contributing to the transport phenomena. Thus

$$1/l = 1/l_B + 1/l_{GB} ,$$

where l_B is a free path for the B-scattering and l_{GB} is that for the GB-scattering. The latter is of the order of the grain size, d_G, while the l value can be calculated based on the carrier concentration and mobility data by using Eq. 1.23. The highest l value we obtained in this way is about 50 Å, while the grain size in our films is in the 10^3 Å scale. Thus $1/l >> 1/l_{GB} \sim 1/d_G$, hence the GB-scattering can be neglected.

A different approach to discussion of the GB influence on the sample resistivity is based on modeling the polycrystalline material as a two-phase system. One phase is the material inside grains (bulk material), and the other (high resistivity) phase is the material in the GB region. When traveling through the sample under the influence of the electric field, an electron is crossing consequently grains and grain boundaries. Hence the electrical circuit of the sample consists of resistors, R_B and R_{GB}, representing bulk material and GB, respectively, and connected in series. When measuring DC resistivity, with either the four probe or van der Pauw method, we measure the sum of these two types of resistances. Thus the Hall mobility in general should be lower or at least the same as the real bulk mobility:

$$\mu_H \approx \frac{\mu_B}{1 + R_{GB}/R_B} \qquad (1.33)$$

Mobility can be also determined by using the effective mass and collision time (momentum relaxation time) values, the latter derived from optical measurement. We call this mobility the optical mobility:

$$\mu_{opt} \approx \frac{q\tau}{m^*} = \frac{q}{m^* \omega_c} \qquad (1.34)$$

Collision frequency is the actual frequency of scattering and is influenced by grain boundaries only if l_{GB} and l_B values are comparable, which is not the case for our films as shown above, hence $\mu_{opt} \approx \mu_B$.

Table 1.3 Comparison of the Hall and optical mobility values.

Sample #	Thickness (nm)	Hall carrier conc. (10^{20}cm^{-3})	Mobility (cm^2/Vs)	
			μ_H	μ_{opt}
1	110	5.9	4.5	21
2	60	4.0	4.5	32
3	90	2.4	3.3	29
4	370	5.6	25	26
5	500	4.6	29	30
6	470	3.1	11.5	12

Table 1.3 presents the Hall and optical mobility values for several typical films. It is seen that for the first three samples (low thickness, small grain size) μ_H is significantly smaller than μ_{opt} which indicates a significant influence of the grain boundaries, while for the last three (larger thickness) these values are practically the same, within the accuracy of measurements and modeling. For these films, the contribution of the GB to the measured resistivity can be neglected. The data on the films like these were used for the analysis of the bulk scattering mechanism.

Bulk Scattering Mechanism

To identify the scattering mechanism we will start with the well known and widely used signatures of the scattering mechanisms, such as the temperature dependence of mobility and scattering parameter, which is defined by Eq. 1.9. If effective mass is independent of temperature, then temperature dependence of mobility is defined by two factors. The first one comes from the temperature dependence of the density of scatterers. It is clear that for scattering by impurities and crystal structure defects the scatterer density does not depend on temperature. This dependence exists only for scattering by phonons whose concentration increases with temperature. The second factor is defined by two issues: (a) relaxation time dependence on energy and (b) temperature dependence of the energy of the carriers that contribute mostly to the transport, <E>. For the non-degenerate carrier gas (classical statistics) this energy is proportional to temperature: $\langle E \rangle \sim k_B T$. For high degeneracy $\langle E \rangle \approx \eta$ and to the first approximation the Fermi level dependence on temperature should be neglected.

Relaxation time dependencies on energy (hence, scattering parameter) and on temperature for various scattering mechanisms were studied theoretically and believed to be defined precisely for the parabolic band model, e.g., see [15, 16]. Below are presented scattering parameter values and temperature dependencies of mobility (the latter for high degeneracy) predicted by theory for the most common scattering mechanisms:

Acoustic phonon scattering: $r = -1/2$, $\mu \propto T^{-1}$;

Optical phonon scattering:
For temperature below Einstein temperature, Θ_E, $r=0$, $\mu \propto \exp(t/\Theta_E)$;
For temperature well above Θ_E, $r=1/2$, $\mu \propto T^{-1}$;

Scattering by the neutral hydrogen-like impurity centers: $r = 0$, $\mu \propto T^{0}$;

Scattering by point defects with the $\delta(r)$-type scattering potential: $r= -1/2$, $\mu \propto T^{0}$;

Scattering by impurity ions with 1/r-type Coulomb scattering potential: $r = 3/2$, $\mu \propto T^{0}$;

We have measured Hall mobility in temperature range of 300 to 500^0C. No dependence on temperature was found. Based on this result we must exclude all the phonon scattering mechanisms and focus on scattering by defects/impurities. For high carrier concentrations like those in our samples, the most probable mechanism is scattering by impurity ions because the density of impurity ions is the same as the free carriers density, or even higher if there is some compensation. To check this assumption we must look at the scattering parameter. Its value determined from Seebeck coefficient measurements is presented in Figure 1.5. The value obtained ($r=0.9\pm0.2$) is higher than the predicted ones for all the mechanisms listed above, except ion impurity scattering. At the same time it is lower than that indicated above for this mechanism. The discussion below is aimed at explanation of this discrepancy.

The Coulomb scattering potential of the impurity ion is screened due to:

1. Polarization of the electronic shells of the atoms surrounding the impurity atom; dielectric constant corresponding to this screening mechanism is the high-frequency dielectric constant, ε_∞ ; its value for SnO_2 is close to 4.
2. Polarization of the lattice (displacement of the lattice ions toward and outward the impurity ion), characterized by ε_L component.
3. Screening by free carriers (SFC): free carriers are pulled closer to impurity ion (if their charge sign is opposite to that of impurity ion) or pushed out (if the charge signs are the same).

In insulators or slightly doped semiconductors the third mechanism of screening can be neglected and the screened Coulomb potential of an impurity atom is described by

$$|U| = \frac{|Q|}{\varepsilon_o r} \qquad (1.35)$$

where $|U|$ is the magnitude of scattering potential, $|Q|$ is the magnitude of the impurity ion charge, r is a distance from the center of the impurity ion, and $\varepsilon_o=\varepsilon_\infty+\varepsilon_L$ is a static dielectric

constant. In SnO_2 $\varepsilon_o \approx 10$. In metals or heavily doped semiconductors the SFC mechanism can play a significant role and the scattering potential is described by:

$$|U| = \frac{|Q|}{\varepsilon_o r}\exp(-r/r_o) \qquad (1.36)$$

where r_o is the screening radius for SFC which is defined for highly degenerate semiconductors by

$$r_o = \sqrt{\left(\frac{\varepsilon h^2}{16\pi^2 m^* q^2}\right)(\pi/3n)^{1/3}}\ ;\ \ r_o = 3.65\times10^{-5}\varepsilon^{1/2}(m_o/m^*)^{1/2}n^{-1/6} \qquad (1.37)$$

The difference between Equations 1.35 and 1.36 leads to the difference in scattering parameter value for the Coulomb potential screened and unscreened with free carriers. To calculate the scattering parameter, r, value for our materials we will use the theory developed in [21-24]. The dependence of relaxation time on energy for scattering by the impurity ions with SFC can be written in the form:

$$\tau(E) = \left(\frac{\varepsilon^2\sqrt{2m^*}}{\pi q^4 N_i \Phi(E_F)}\right)E^{3/2} \qquad (1.38)$$

where

$$\Phi(E_F) = \ln(1+\xi) - \frac{\xi}{1+\xi}; \qquad \xi = (2k_F r_o)^2 \qquad (1.39)$$

$$k_F = (3\pi^2)^{1/3} n^{1/3} \qquad (1.40)$$

Function $\Phi(\xi)$ in Eq.1.38 reflects the influence of SFC; k_F (Eq.1.40) is the Fermi wave vector magnitude. Based on Eqs.1.38 and 1.39, as well as on the definition of scattering parameter, (see Eq.1.9), we have derived the expression for the scattering parameter for the scattering mechanism under consideration:

$$r = \frac{3}{2} - \frac{d\ln\Phi}{d\ln\xi}\Big|_{E=\eta} = \frac{3}{2} - \frac{\xi^2}{(1+\xi)^2}\frac{1}{\Phi(\xi)} \qquad (1.41)$$

The scattering parameter values calculated for $n=1\times10^{20}cm^{-3}$ and $n=5\times10^{20}cm^{-3}$, $m^*=0.275m_o$, and $\varepsilon=\varepsilon_o=10$ are presented below:

$\underline{n=1\times10^{20}cm^{-3}}$: $\eta=0.26$ eV; $k_F=1.5\cdot10^7$ cm^{-1}; $r_o=10.2$ Å $\Rightarrow$ $\underline{r=0.9}$

$\underline{n=5\times10^{20}\ cm^{-3}}$: $\eta=0.76$ eV; $k_F=2.5\cdot10^7$ cm^{-1}; $r_o=7.5$ Å $\Rightarrow$ $\underline{r=1.0}$

The obtained values of the scattering parameter are close to those obtained from the Seebeck coefficient data (see Fig.1.5). At the same time, based on the values of screening radius, r_o, one can see an additional problem to be discussed. Indeed, due to the screening by free carriers, the scattering potential (see Eq.1.36) turned out to be localized in the region of the order of the unit cell. If so, the problem is what dielectric constant value should be used when calculating r_o and τ. The screening effect caused by displacement of the lattice ions, Sn^{+4} and O^{-2}, depends on how many coordination spheres are involved in the ionic screening. To provide the effect corresponding to the "static dielectric constant", ε_o, the ion displacement must occur in

many unit cells surrounding the impurity atom. This is not the case if the perturbing potential is located in the region close to one unit cell. Thus we must suggest that the effective dielectric constant that should be put in our calculations is lower than ε_o. Therefore we have recalculated r_o and scattering parameter with $\varepsilon=\varepsilon_\infty=4$ (the lowest possible ε value) . The results are as follows:

$n=1\times10^{20}cm^{-3}$: $r_o=6.5$ Å $\Rightarrow$ $r=0.7$; $n=5\times10^{20}\ cm^{-3}$: $r_o=4.8$ Å $\Rightarrow$ $r=0.8$

It is seen that the scattering parameter does not change considerably and stays close to the experimental value. The real effective dielectric constant should be somewhere between ε_o and ε_∞, hence the scattering parameter between the values calculated for the limiting ε values. Thus one can conclude that the dominating bulk mechanism of scattering is the scattering by impurity ions screened with free carriers.

Calculation of Mobility in the Bulk of the Grains

Studies presented above provided us with the information that allows calculating the carrier mobility and comparing the calculated and measured data. For calculations the equation

$$\mu = q\tau(\eta)/m^*(\eta) \qquad (1.42)$$

was used where the effective mass was assumed to be isotropic, independent on carrier concentration (hence on $\eta=E_F-E_C$) and equal to 0.275 m_0. Relaxation time, which generally depends on carrier concentration that is on η, was calculated by using Eqs.1.38-1.40. Carrier concentration was assumed to be $=5\times10^{20}cm^{-3}$ which is close to that for the best SnO_2 TCO samples. The Fermi energy value, η, corresponding to this concentration, calculated by using Eq. 1.18, is equal to 0.76 eV. Because of the uncertainty in the effective dielectric constant value (due to the spatial dispersion) mentioned above, we calculated μ value for different ε in the range from ε_∞ to ε_o. The results of calculations are presented in Table 1.4. We assumed no compensation, that is the density of scatterers, N_i in Eq.1.38, is equal to the carrier concentration.

Table 1.4 Calculated mobility as a function of dielectric constant. $n=5\times10^{20}$ cm^{-3}; compensation degree $\beta=0$

ε	r_o (Å)	μ ($cm^2/V\cdot s$)
10	7.2	83
8	6.7	60
6	5.8	40
5	5.3	32
4	4.8	23

It is seen from the table that (a) the SFC screening radius, r_o, is really small, hence we need to use dielectric constant value lower than ε_o, and (b) mobility calculated with $\varepsilon=5$ is close to the experimental data (around 30 cm^2/Vs). If the measured mobility is so close to theoretically calculated, then one may conclude that the achieved level of mobilities is close to the limiting one, and there is no much room for the mobility increase by improvement of processing technology. A conclusion of this kind would be of great importance for industry if there were not some uncertainty about the dielectric constant value that should be used for calculation of mobility.

Another source of uncertainty is the compensation problem. One can not be sure that the compensation degree for the samples we studied experimentally was zero. If the compensation is considerable, then in our calculations of mobility we must use the density of the scatterers greater than the carrier concentration. Indeed, $N_i=N_d+N_a$, $n=N_d-N_a$, where N_d, Na, and N_i are the densities of donors, acceptors and impurity ions, respectively. If we designate the compensation degree as $\beta\equiv N_a/N_d$, and mobility in the non-compensated material ($\beta=0$) as μ_0, then the mobility in compensated material with the same carrier concentration, $\mu(\beta)$, can be written as

$$\mu(\beta)=\mu_0[(1-\beta)/(1+\beta)] \qquad (1.43)$$

It is seen from this equation that even for a non-significant compensation degree, the measured value of mobility could be considerably lower than that for the uncompensated material with the same carrier concentration. Table 1.5 shows the calculated decrease in mobility due to increase in compensation degree for the given donor concentration.

Table 1.5 Calculated ratio of mobilities in compensated and uncompensated SnO_2 for the same donor concentration, $N_d=5\times10^{20}cm^{-3}$.

Comp. degree (β)	Carrier Conc. (n, $10^{20}cm^{-3}$)	$\mu(\beta)/\mu_0$
0.0	5	1
0.2	4	0.7
0.4	3	0.48
0.6	2	0.3
0.8	1	0.15

Unfortunately our deposition system did not permit precise control of the fluorine dopant content. We also could not measure directly donor and acceptor concentrations in the prepared films. However as an indirect evidence of the compensation influence we will present below the data on mobility for several samples with different carrier concentrations.

To exclude a possible influence of grain boundaries we selected samples for which the Hall and optical mobilities differ only slightly from each other (less than 7%). We compared two groups of samples prepared at different times and under slightly different conditions. The first group consists of three samples with almost the same parameters: thickness (averaged thickness $\langle t\rangle$=450 nm), carrier concentration ($\langle n\rangle=5.3\times10^{20}cm^{-3}$), and mobility ($\langle\mu\rangle$=29.6 cm^2/Vs). The other group also consists of three samples with common parameters and is characterized by $\langle t\rangle$=510 nm, $\langle n\rangle=3.1\times10^{20}$ cm^{-3}, and $\langle\mu\rangle$=12.6 cm^2/Vs. Calculation of mobility based on the assumption of zero compensation for both groups leads to a mobility value higher for the first group by only about 10 % because of higher concentration and more pronounced SFC. Let us now suppose that compensation is absent in the first group ($N_{d1}=n_1$), and the donor concentration in the second group is the same as in the first one ($N_{d2}=N_{d1}=N_d$). If so, compensation is the only reason why in the second group carrier concentration is lower, and compensation degree can be estimated as $\beta=(N_d-n_2)/N_d=(n_1-n_2)/n_1=$ 0.42. According to calculations like those presented in Table 1.5, the ratio of mobilities should be: $\mu_2/\mu_1=0.45$ which is in a good agreement with the experimental ratio, 0.425.

If all the samples we studied experimentally were compensated, then we must compare the theoretically calculated mobility with the measured value corrected by a factor $(1+\beta)/(1-\beta)>1$. In this case, the coincidence of the calculated and corrected experimental data will take place at higher values of the effective dielectric constant, ε. Thus there are two sources of the uncertainty when calculating mobility: (a) spatial dispersion of dielectric constant that should be analyzed theoretically in the future studies; (b) possible influence of compensation which should be studied experimentally.

1.5 Comparison of Different Methods of Characterization

For high scale manufacturing of TCOs, routine testing techniques necessarily include sheet resistance and spectral transmission measurements. Often people need much more detailed information on the properties of the films in connection with the varying preparation conditions, especially at the stage of research and development. For applications where high transparency and conductivity are required it is desirable to maximize the ratio of electron mobility to carrier concentration. Measurements of sheet resistance or even bulk resistivity themselves do not allow us to separate these parameters, and we need additional measurements. Resistivity in polycrystalline materials can be greatly influenced by the presence of the grain boundaries, gaps between grains, voids, etc. It is desirable to estimate the influence of these factors. In this study we have used various methods and techniques for determination of the same parameters, e.g., the Hall and Seebeck effects and plasma frequency for measurement of the free carrier concentration, or Hall plus resistivity and collision frequency for determination of the carrier mobility, etc. In this section we will try to compare various methods for TCO thin film characterization and discuss their advantages and shortcomings based both on theory and on our own experience of their application.

Carrier Concentration

Hall effect measurement is the most direct method for determination of the free carrier concentration. It is easy to apply to the TCO thin films. However there are several sources of inaccuracy and uncertainty when using this method. If the carrier concentration fluctuates spatially, but the sample is uniform in all other respects, the Hall measurement provides concentration value averaged over the sample volume. But, if mobility is laterally non-uniform (which often occurs in thin films), the average carrier concentration is underestimated. Inaccuracy can increase due to not well-defined geometry of a sample, non-uniformity of its thickness, presence of voids, microcracks, and gaps between grains. It should be also mentioned, that the Hall method is destructive (we need to cut from the whole produced plate a small sample of a regular shape and solder to it electrical contacts).

Seebeck effect measurement is an indirect method for the carrier concentration determination. It could be used routinely if S(n) dependence is empirically established by means of comparative measurements of the Hall and Seebeck on the series of high quality samples with different carrier concentrations. If we have a reliable S(n) calibration, then we can replace the Hall measurements by the Seebeck measurements. Some important features and advantages of the Seebeck coefficient measurements should be mentioned and discussed here:

1. The Seebeck coefficient measurements do not demand some special geometry of the sample and can be performed on the samples of an arbitrary shape and size and even on the samples of non-uniform thickness.
2. The measured Seebeck coefficient is not influenced significantly by the voids, microcracks, grain boundaries. For samples containing such kinds of defects, information obtained about the carrier concentration by using S(n) calibration curve can be more reliable than that obtained from the direct Hall effect measurements.
3. Only those portions of the sample material, where the temperature gradient exists, contribute to the measured Seebeck voltage, V_S. For our arrangement where the entire sample is held at room temperature, except the region close to the heated copper block, only the material located in the vicinity of the block contributes to the measured signal. Thus, if the block is sharpened (thermoprobe), we are able to measure the local Seebeck coefficient. The spatial resolution is on the order of the size of the contact between the thermoprobe and a sample. It could be easily made less than 1 mm. By relocation of the thermoprobe on the film surface we can map the Seebeck coefficient (and hence the carrier concentration) distribution over the sample area.
4. This method is not destructive: the measurements can be performed on the produced plate; putting the reference electrodes (copper blocks in our equipment) on the sample surface and relocating them does not damage the film.
5. Each measurement of the local Seebeck coefficient takes a short time if the temperature of measurements is close to room temperature and the tools for measurement are like those described in Sec. 1.2.

Plasma frequency measurements also can be used to get information on carrier concentration. This method is also indirect, similarly to the Seebeck measurements. The equation, which relates plasma frequency to the carrier concentration, is simpler than that for the Seebeck coefficient. The only parameter we need to know to calculate the concentration from the ω_p data is the effective mass. If this parameter is not well defined, an empirical approach can be used as in the case of the Seebeck effect. Comparative measurements of plasma frequency and the Hall concentration should be conducted on a series of high quality samples with varying carrier concentration to obtain $n(\omega_p)$ calibration.

Plasma frequency can be determined from the location on the wavelength scale of a sharp increase in reflectance. Our studies demonstrated that the reflectance increase for heavily doped SnO_2 samples is sharp enough for the satisfactorily accurate ω_p determination. More accurate data can be obtained when modeling the reflectance and transmittance spectra based on the Drude model. Including the Lorentz oscillators into the model should in principle improve the theory and experiment fitting, but in our studies no considerable manifestations of the Lorentz oscillators were observed.

To determine ω_p we used not only a reflectance spectrophotometry but also multi-angle spectral ellipsometry. The latter derives its sensitivity, which is greater than a simple reflection measurement, from determination of the relative phase change in a beam of reflected polarized light. Ellipsometry is more accurate than reflectance intensity measurement because the absolute intensity of the reflected light does not have to be measured. There was a good agreement between parameters obtained with ellipsometry measurements and those obtained from the

reflectance spectra. The modeling we used for ellipsometry provided an opportunity also to reveal non-uniformity in ω_p over the film thickness. This was used to screen samples when we selected the uniform samples for the comparative Hall, Seebeck and plasma frequency studies. In general, this method can be used if non-uniformity is the issue to be detected and studied.

As compared to the Seebeck effect, the optical methods have some shortcomings. While the former can be applied to samples of unlimited sizes, the equipment used for optical characterization puts some limitation on the sample size. Samples with area not higher than 2"×4" could be tested in our spectrophotometer and for the ellipsometry the limitation was 12"×12". Spatial resolution, for the Seebeck measurements, is determined by the sharpness of the thermoprobe tip. The diameter of the contact spot can be easily made less than 1 mm. As to optical testing, the spatial resolution is limited by the light beam cross section. The measurements and the raw data treatment are much easier for the Seebeck measurements. The equipment/tools for these measurements are much simpler, less expensive and more durable.

A more fundamental limitation on the optical methods application comes from the spectral range of the instruments we use. Our instruments cover visible light range, near UV and near IR ranges, e.g., the spectral range of our spectrophotometer is of 250 to 2500 nm. For the SnO_2 samples with carrier concentration in the range of 1×10^{20} to $6\times10^{20}cm^{-3}$, the plasma frequency could be measured with an acceptable accuracy. As the concentration decreases, the plasma frequency shifts farther to the IR range ($\omega_p \propto n^{1/2}$) and the accuracy drops. For the concentrations below 1×10^{19} cm^{-3}, measurements of ω_p become unreasonable unless we use a spectrophotometer for the far IR.

Carrier Mobility

Usually mobility is defined as $\mu = (q \cdot n \cdot \rho)^{-1}$, where n is the carrier concentration and ρ is the measured electrical bulk resistivity. Concentration can be determined by the Hall, Seebeck and plasma frequency measurements as discussed above. Electrical resistivity measured by common DC or low-frequency AC methods is often overestimated. If the sample structure is not perfect, especially if the sample is not a single crystal, imperfections can contribute much to the measured ρ value. The presence of voids, microcracks, non-uniformity of the film thickness or even the surface roughness increase the resistance of the sample and lead to underestimation of the carrier mobility of the substance. In a polycrystalline material, grain boundary regions can be much more resistive than the material inside the grains. Studies of CdTe and CdS thin polycrystalline films have shown that the mobility determined through DC measurements of resistivity can be by orders of magnitude lower than the real mobility of the carriers inside the grains. High-frequency (up to tens of MHz) AC measurements we use in our laboratory provide an opportunity to separate the individual contributions to the resistance of grain boundaries and intragrain material. The electrical equivalent circuit for the grain boundary region contains a resistor and capacitor connected in parallel. The former at high frequencies is shunted by the latter and becomes much lower than the intragrain resistance. Unfortunately, this method could not be applied to the TCOs where the resistance of the grain boundaries turned out to be very small and shunting by capacitance is not effective.

Another approach for the real intragrain material mobility measurement was used in this research which was based on optical characterization of the material. Carrier mobility can be calculated if the effective mass value and collision time (momentum relaxation time) are known: $\mu = q\ \tau\ /\ m^*$. We have determined the m^* value from $\omega_p(n)$ dependence which is in a good

agreement with the literature data. Collision time was determined by the spectroscopic ellipsometry measurements as a reciprocal of the collision frequency: $\tau = \omega_c^{-1}$. To distinguish the mobility value obtained in this way we designate it as μ_{opt} contrary to the Hall mobility, μ_H.

Collision frequency is defined by all the collision (scattering) processes which lead to the dissipation of the electron momentum, hence μ_{opt} is a real mobility inside the grain material. Grain boundaries do not influence this parameter if the grain size is much greater than the mean free path length, hence μ_{opt} can be higher (or even much higher) than μ_H.

Which of the two methods for the mobility determination should be used, depends of the objectives of the material characterization. The optical mobility and optical resistivity, $\rho_{opt} = (q \cdot n \mu_{opt})^{-1}$, are the real mobility and resistivity of the intragrain material. The DC resistivity is a characteristic of the film itself with all the structural defects like grain boundaries, voids, etc., and defines the TCO quality with respect to technical applications.

Limitations on "optical" mobility measurements are the same as for the plasma frequency. Collision frequency is derived from the spectral optical characteristics in the spectral range close to the plasma frequency.

Film Thickness and Surface Roughness

Film thickness and roughness were measured by means of the Surface Profiler and also by using the ellipsometry. The results obtained by these methods are in a satisfactory agreement with each other for the films with a thickness in a range which is typical for the technical applications, that is above 350 nm. For films with thickness of around 100 nm, agreement was much worse. It is difficult right now to conclude which method is more accurate, but reproducibility was better for the ellipsometry measurements. Another advantage of ellipsometry is that this is a non-destructive method while measurements with the profiler demanded removal of some portion of the film to provide a step whose height was measured by the profiler.

Conclusions

- Various methods of material characterization can be used for getting an information on optical, electrical and structural properties of TCO thin films.
- In addition to common Hall effect measurements, carrier concentration can be derived from Seebeck coefficient, S, measurements by using S(n) calibration. This is a reliable, non-destructive method that can be applied to the thin film samples of an arbitrary shape and size and to materials in a wide carrier concentration range. Relocation of a sharpened thermoprobe over the film surface allows to measure and map local carrier concentration. In combination with the four-point probe measurements of sheet resistance it also provides an opportunity to map local mobility.
- Optical characterization can provide an information not only on optical properties of the material (spectral transmittance, reflectance and absorbance) but also on the electronic parameters, such as carrier concentration and mobility. The latter two can be derived from plasma frequency and collision frequency with modeling based on the Drude model.
- Comparison of the Hall and optical mobility values is the basis for estimates of grain boundary contribution to the measured DC resistivity of a sample.

- Multiangle spectral ellipsometry provides wide options for material characterization. From these measurements the data can be derived on carrier concentration, mobility in the intragrain material, film roughness and thickness, as well as optical transmittance, reflectance, absorbance, and dielectric constant. This method is the most preferable for characterization and studies of multilayer materials, like TCO/buffer layer/insulating substrate (glass or polymer).

1.6 Major Results

1. SnO_2: F thin films on soda lime glass substrates were prepared using APCVD technique with transparency and sheet resistance close to those for the best commercially available materials.
2. A variety of methods were used to characterize electronic properties of the films, including:
   - Sheet resistance (four-point probe measurements)
   - Hall effect, Hall mobility and bulk resistivity (van der Pauw geometry)
   - Seebeck coefficient (thermopower)
   - Plasma frequency and collision frequency (spectrophotometry and multiangle spectral ellipsometry.
3. The results of combined electrical and optical measurements were analyzed based on the electron transport theory specialized for the highly degenerate electron gas. In this way basic parameters of the electronic system were determined:
   - Effective mass in a wide energy range; no indications of non-parabolicity were found
   - Contribution of grain boundaries to the total film resistance in plane, which was found almost negligible for the films with high mobility
   - Mobility inside the grains and dominating scattering mechanism (by impurity ions strongly screened with free carriers
4. For this scattering mechanism, bulk mobility was calculated which turned out to be close to the experimentally determined one if one assumes the effective dielectric constant is close to 5, that is significantly lower than the static dielectric constant for this material ($\varepsilon_0 \approx 10$). This result seems reasonable if to take into account that the free carrier screening radius and localization of the perturbing impurity ion potential are close to the unit cell size. That makes screening with displacement of the host ions less effective (spatial dispersion of dielectric constant).
5. Possible effect on mobility of the donor dopant compensation by native defects was estimated. It was shown that eliminating compensation is an important issue for preparation of TCO films with high mobility (low sheet resistance).
6. Various methods for TCO thin films characterization were compared, their advantages and shortcomings were analyzed.

2. AC Electrical Characterization of CdTe and CdS Thin Films

2.1 Introduction

Measurements of the complex impedance (Z) on polycrystalline films are aimed at separation and independent studies of grain boundaries (GB) and intragrain (IG) material. The basic idea of the method is that a polycrystalline film consists of two phases with very distinct electrical properties. One phase is the IG material and the other is presented by the GB regions with the potential barriers for the majority carriers. GB is characterized by high resistance and also by capacitance provided by a depletion semi-insulating regions adjacent to the GB. The grain is assumed to be electrically equivalent to a resistor, whereas the GB is electrically modeled as a resistor in parallel with a capacitor. At low frequencies the film impedance is almost totally defined by the GB resistance. At high frequencies the GB capacitor effectively shunts the GB resistor, so that the measured resistance tends to the IG resistance. Thus measurements in a wide frequency range provide an opportunity to separate individual contributions of GB and IG material to the sample resistance and determine the GB capacitance. The method proved to be effective for studies of CdTe thin films on insulating substrates [25, 26]. GB resistance and capacitance are to be studied under different conditions, such as temperature, illumination intensity and spectrum, and bias. These studies presumably should provide information on the electronic properties of the GB, like potential barrier height, doping level in the vicinity of GB, density of GB states, etc. Knowledge of these properties that can vary under different processing procedures, is important for understanding the influence of grain boundaries on solar cell performance and developing new approaches to improvement of the cell quality.

In order to be able to measure complex impedance/admittance, an LCR meter (Hewlett Paccard 4285A) and an HP-VEE (Visual Engineering Environment) software have been purchased.

The instrument provides measurements in the frequency range from 75 kHz to 30 MHz; the software runs the LCR meter using HP-IB communicating standard. Using this software, about 20 experimental procedures have been developed, which enabled us to run a variety of experiments for measurement of different electrical parameters of a sample. The main measurement types performed routinely are:

1. Impedance magnitude, $|Z|$, and phase angle, Θ, as functions of frequency.
2. Real, Re(Z), and imaginary, Im(Z), parts of impedance as functions of frequency.
3. Resistance and capacitance as functions of frequency.
4. $|Z|$ and Θ as functions of bias voltage.
5. Re(Z) and Im(Z) as functions of bias voltage.
6. Resistance and capacitance as functions of bias voltage.
7. Im(Z) as a function of Re(Z) ("Impedance Spectroscopy").
8. Resistance and capacitance as functions of time after switching on and off light or bias (transient processes).

All the parameters listed above characterize a sample as a whole. These parameters should be analyzed based on the physical and mathematical models that represent to some approximation real electronic properties of a polycrystalline thin film. This is a major goal of the studies presented in this report. We started with the simplest model (equivalent electrical circuit) and found that fitting of the model with experimental results is satisfactory which enabled us to estimate the GB resistance and capacitance as well as resistance of the IG material. Then we went further, using more complicated electrical circuits and sophisticated physical models that led to more precise fitting of the data and provided more detailed information on the GB electronic properties and electronic processes that occur at the GB region. Based on the same approach, we will continue our studies developing new experimental procedures and new models as we obtain new results on films differently prepared and treated.

2.2 Film Resistance and Capacitance at Zero Bias. A Simple Electrical Circuit Model

Preliminary measurements aimed at comparison of different measurement procedures and approaches to the results treatment were performed on CdTe and CdS thin films. CdTe films were prepared with physical vapor deposition on glass substrates (IEC at the University of Delaware) and treated in different ways at CSM. CdS films were deposited on glass substrates by CBD and treated at our facilities. The evaporated golden strips were used as electrodes providing semi-ohmic, low resistance electrical contacts to CdTe and high resistance rectifying contacts to CdS. In complete darkness the samples usually exhibit a very high resistance that makes impossible accurate measurements in the whole frequency range. To avoid this, we used to perform measurements under illumination that provides a controllable lowering of the GB resistance. The results of measurements were being compared with those calculated for an equivalent circuit consisting of "blocks", each block is a GB resistor R_1 in parallel with a GB capacitor C_1, both in series with another, IG resistor R_2. One block represents one grain with one grain boundary. In reality, any sample is made of thousands of these blocks.

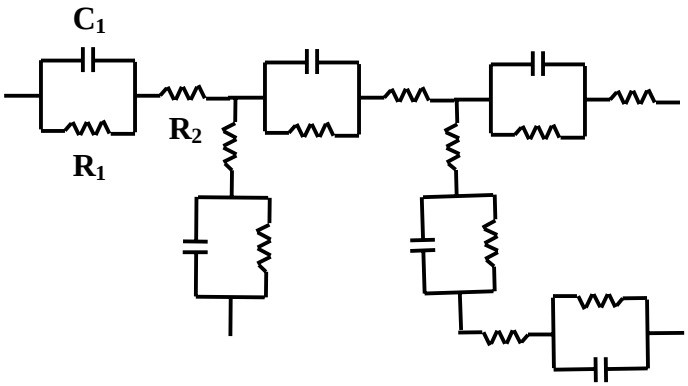

Figure 2.1 Fragment of the thin film equivalent circuit

Measuring the electrical resistance and capacitance of CdTe and CdS samples with assuming an equivalent circuit of only one block (Fig. 2.2), yielded a reasonably good fit to the calculated data (Figs. 2.3 and 2.4). Measurements were done in two LCR meter modes: "p" which suggests that the circuit is composed of a resistor and capacitor in parallel, and "s" which suggests the circuit composed of a resistor and capacitor in series.

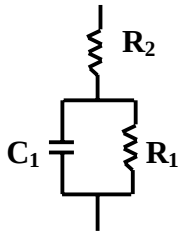

Figure 2.2 One block equivalent circuit. R_1 and C_1 represent resistance and capacitance of the whole grain boundary network. R_2 represents resistance of the intragrain material

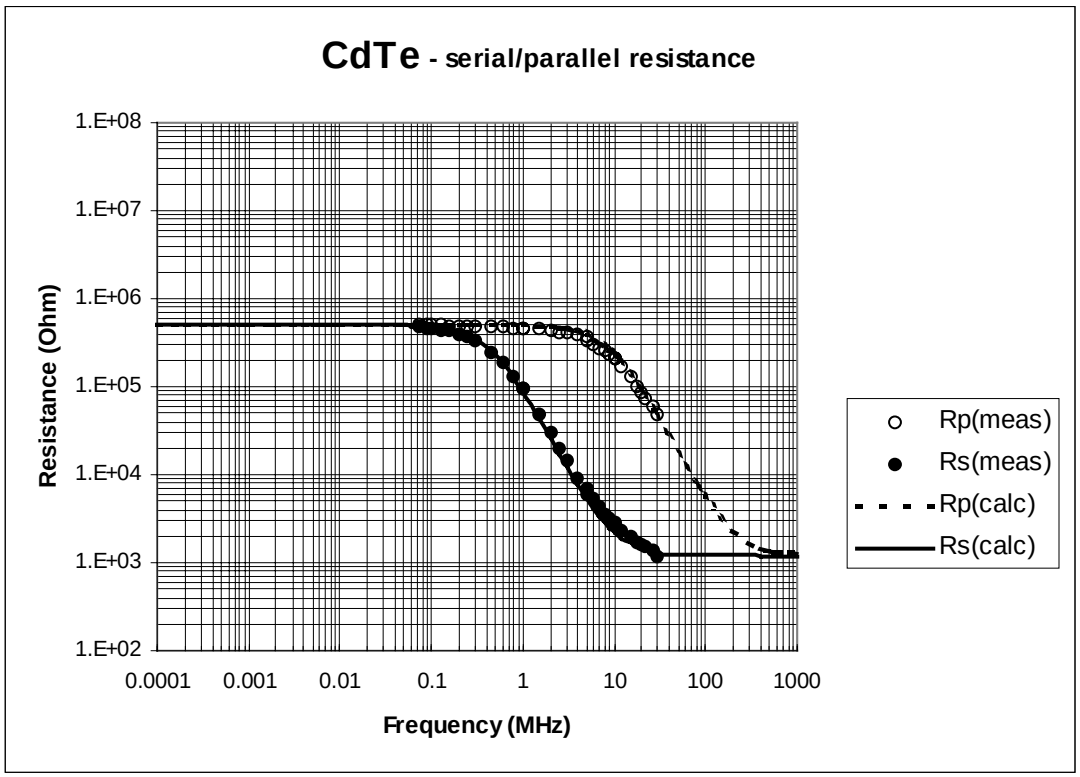

Figure 2.3 Experimental results for the resistance of a CdTe layer demonstrating the fit to a simple one-block equivalent circuit

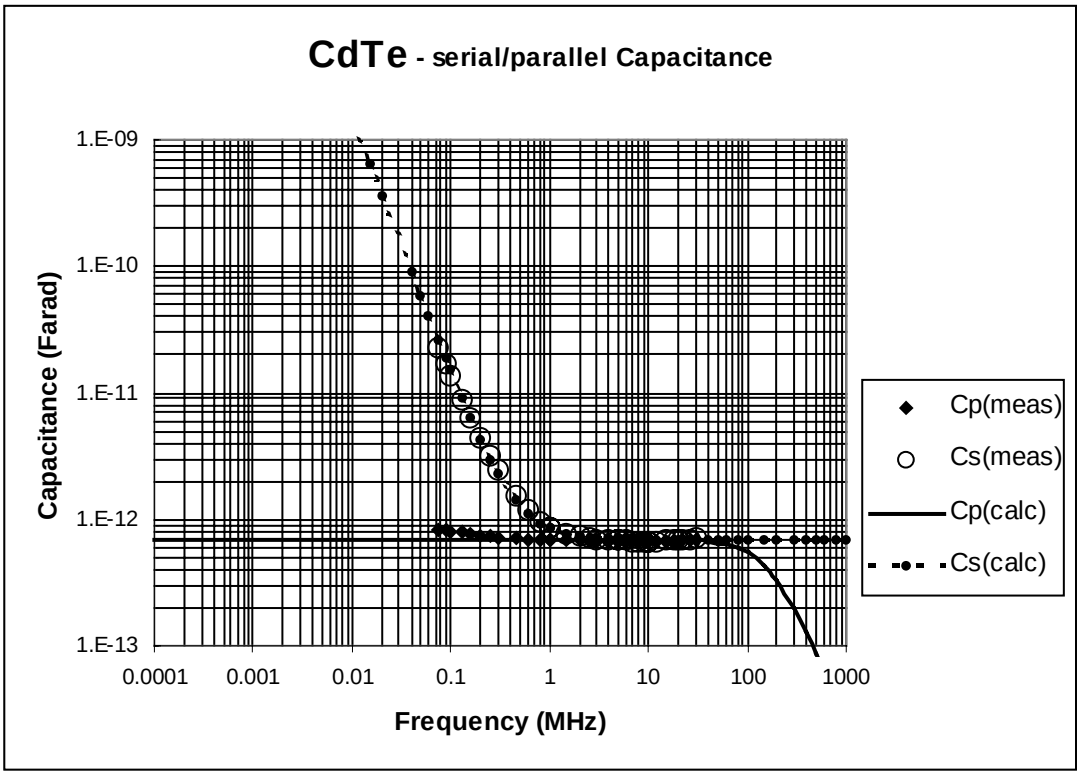

Figure 2.4 Experimental results for the capacitance of a CdTe layer demonstrating the fit to a simple one-block equivalent circuit

Relations between the displayed R_p, C_p, R_s and C_s values, and the sample parameters, R_1, C and R_2 derived from the impedance and admittance analysis for the circuit in Fig. 2.2 are as follows:

$R_p=R_2+[R_1/(1+\alpha)]\cdot\{1+\alpha/[1+(R_2/R_1)(1+\alpha)]\}$; $C_p=C\cdot(1+\alpha)/\{[1+R_2/R_1(1+\alpha)]^2+\alpha$;

$R_s=R_2+R_1/(1+\alpha)$; $C_s=C\cdot(1+\alpha)/\alpha$;

where $\alpha=(R_1C\omega)^2$ and ω is an angular frequency.Good fitting means that using "lumped" parameters is an acceptable procedure for these measurements, and that in our case, a single block may represent quite adequately a polycrystalline material composed of a lot of grains. The fitted results make it possible to extract R_1, C_1 and R_2 from the measurements.

Incorporating more than one block yielded even better fits, which gives a simple means for evaluating the range of distribution of the values of these parameters. Very good fitting was found when three blocks were incorporated with the same C_1 and R_2 values while R_1 values for the three blocks related to each other as 1:1.5:2. Since resistance of the GB depends exponentially on the barrier height, it may be concluded that standard deviation of the latter from the average is very small.

The same parameters can be yielded by other frequency dependence measurements, e.g., Re(Z) and Im(Z) or $|Z|$ and Θ. What kind of measurements is preferable depends on the relations

between values of R_1, R_2 and C. A very helpful and attractive method is measurement of Im(Z) as a function of Re(Z). This measurement yields a graph that has a semi-circle shape (see Fig. 2.5).

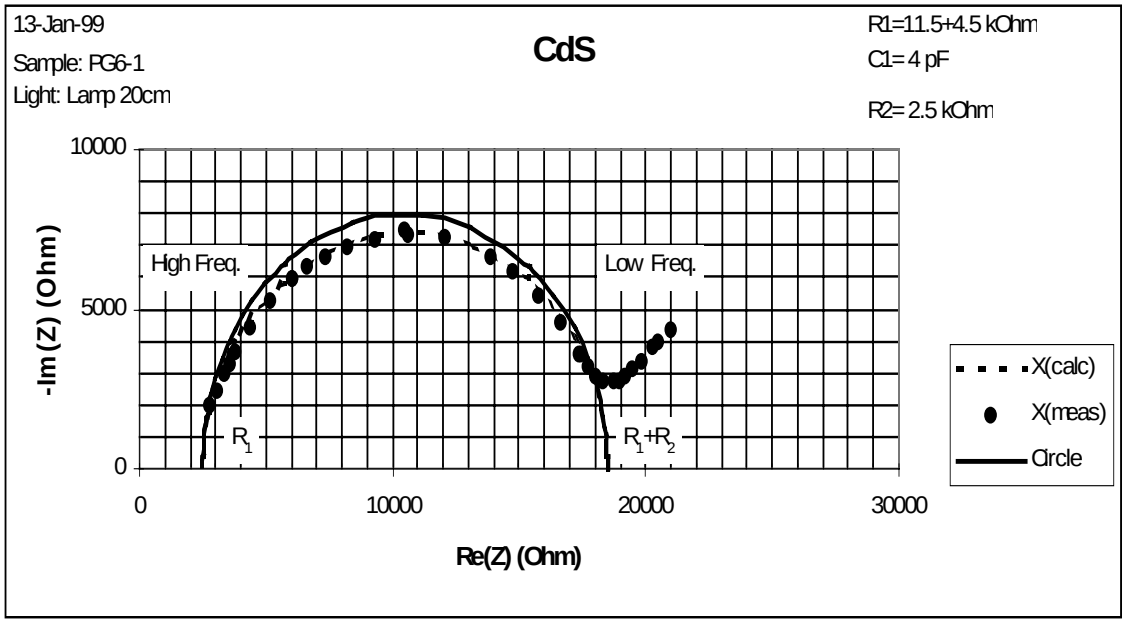

Figure 2.5 Impedance spectroscopy of a CdS layer. Solid line shows a semi-circle representing calculation for one block circuit. Dotted line shows calculation for two-block circuit, which demonstrates a spread in R_1 of about a factor of 2.5. The tail at low frequencies is attributed to the electrodes.

This feature makes it very convenient for analysis. For the simple, one-block equivalent electrical circuit, the maximum value of Im(Z) is equal to $R_1/2$; intersection of the graph with the Re(Z) axis at high frequency yields the R_2 value; the angular frequency, ω_0, at which maximum Im(Z) is observed, provides the C_1 value: $C_1=(R_1 \cdot \omega_0)^{-1}$.

Incorporating more than one block yielded even better fits, which gives a simple means for evaluating the range of distribution of the values of these parameters. Another advantage of this method is the ability to eliminate the contribution of high resistance electrode contacts to the derived thin film parameters. To include these contacts, our equivalent electrical circuit must be composed of two blocks connected in series. The first one (R_1, C_1, R_2, as before) represents the film between the electrodes; the second (R_{cont}+C_{cont} in parallel) represents contacts. The total measured impedance is the sum of those for the two blocks. Each block itself provides a semicircle dependence of Im(Z) on Re(Z), but the frequencies corresponding to their maxima, ω_0^{film} and ω_0^{cont} , may be quite different. The large area contact capacitance, C_{cont}, is orders of magnitude higher than that of the film. If the contact resistance is comparable or higher than that of the film, then $\omega_0^{film} >> \omega_0^{cont}$, contribution of the contacts to the impedance is negligible in the frequency range around and above ω_0^{film} , and the parameters R_1, R_2 and C derived from the measurements are not influenced by the contacts (see Fig. 2.5). This feature may make a four-point measurement unnecessary.

The results presented above (R_{GB}, R_{IG}, C_{GB} values and their dependence on illumination) enable us to make some qualitative conclusions and numerical estimates of the electronic properties of the films.

1. The contribution of the IG material to the total measured resistance is 10^3-10^6 times lower than that of the GB, so that this resistance is almost totally defined by the GB. The GB potential barrier height, ϕ_B, values estimated based on the thermionic emission theory are of the order of several tenths of an electron-volt, in agreement with the estimates in [26].

2. Capacitance, *C*, of a sample is mostly defined by the capacitance of the GB regions. Capacitance measured on the CdTe sample treated with $CdCl_2$ was about 10^{-12}F. The film thickness, *t*, was about 3.5 μm, distance between gold electrodes, *l*, was 0.2 mm, the size of the sample in the third direction, *b*, was about 1cm, the average grain size, *d*, was about 3μm. If we simplify by assuming that the film consists of the square shaped grains of the same size, *d*, then a specific capacitance (per unit area) of a single GB, C_{sp} can be estimated as

$$C_{sp} = C\frac{1}{bt}\frac{l}{d} \qquad (2.1)$$

For the film parameters listed above, one obtains $C_{sp} \approx 4\times10^{-7}$F/cm^2. Knowledge of the specific capacitance and the barrier height enables us to estimate the doping level, N_D, in the GB vicinity. Indeed, $C_{sp}=\varepsilon\varepsilon_0/2W_{GB}$, where W_{GB} is a depletion width on each side of a GB which depends on Φ_B and N_D: $W_{GB}=(2\varepsilon\varepsilon_0\Phi_B/qN_D)^{1/2}$. Thus we have:

$$N_D,\text{cm}^{-3}=5.66\times10^{32}\times\varepsilon^{-1}\times(\Phi_B/e),\text{V}\times(C_{sp},\text{F/cm}^2) \qquad (2.2)$$

Taking $\varepsilon\approx10$ for CdTe and assuming $\Phi_B/e\approx0.5$V, we obtain $N_D\approx1\times10^{18}$cm^{-3}. This number is three orders higher than the CdTe doping level value that is obtained by C-V measurements on CdTe/CdS solar cells. Let us suppose that due to simplified topography of GB network we overestimate C_{sp} value by the factor of 2. Even then we have $N_D\approx2.5\times10^{17}$cm^{-3}, which still significantly exceeds the C-V data. L. Woods [26] has also concluded that doping level in the vicinity of GB in CdTe is on the order of 10^{17}cm^{-3}. He derived his estimates from analysis of temperature dependence of the GB conductance based on a thermally-assisted tunneling model.

3. The IG material resistivity estimated from our measurements is of the order of 10 Ω-cm. Resistivity calculated as $\rho=(qn\mu)^{-1}$ has a value of ≈100Ω-cm for $n=10^{15}$cm^{-3} and mobility as high as 60 cm^2/Vs which is the highest hole mobility value measured in CdTe single crystal. High doping level in the GB vicinity may be a possible reason for this discrepancy. Indeed, the high conductivity layers along the grain boundaries parallel to the current direction can effectively increase the conductance of the grains, so that the effective IG resistivity decreases.

4. All CdTe and CdS films demonstrated high photoconductivity. This effect is more pronounced for films that have a higher dark resistance. By varying the illumination intensity (usually we it was not higher than 0.125 Sun) we were able to decrease R_1 by orders of magnitude, while R_2 was almost not effected and remained orders of magnitude lower than R_1. The measured film capacitance demonstrated only a small increase under illumination that did not exceeded 10-15%. These results leadsto the following conclusions:

- The high photoconductive effect in polycrystalline CdTe and CdS thin films is totally due to a decrease in the GB resistance. The latter depends exponentially on Φ_B, therefore even a small

change in Φ_B caused by light can lead to a dramatic change in R_{GB}. For example, for $\Delta\Phi_B \approx 0.1$ eV, one has at room temperature $\Delta R_{GB}/ R_{GB} \approx 50$. The GB depletion layer width is proportional to $\phi_B^{1/2}$, so that 10% increase in C corresponds to 20% decrease of ϕ_B.

- Illumination with the intensity we used (<1Sun) does not lead to a remarkable increase in carrier concentration inside the grains. This conclusion is consistent with doping level ($\gtrsim 10^{14}$-10^{15} cm^{-3}) in our films and the lifetime for the photogenerated carriers (~10^{-9} sec) derived from PL intensity decay.

2.3 Changes in the Film Electrical Parameters under Applied Bias

Repeating measurements with the application of a DC bias, showed that the film parameters, R_1 and C_1, are dependent on the applied voltage. The procedures 4-6 in the list presented above made it possible to measure the sample electrical parameters at various biases. The results demonstrated a strong dependence on bias particularly in the lower frequency range. This dependence becomes less and less pronounced and then vanishes as frequency increases (see, e.g., Figures 2.6 and 2.7). X(Z)-R(Z) plots also demonstrate a considerable increase in film resistance and capacitance. Changes in the GB resistance and capacitance may be attributed to the increase of electrical charge accumulated in the GB states under influence of bias. This effect was discussed and analyzed in numerous publications, see, e.g., [27, 28, 31].

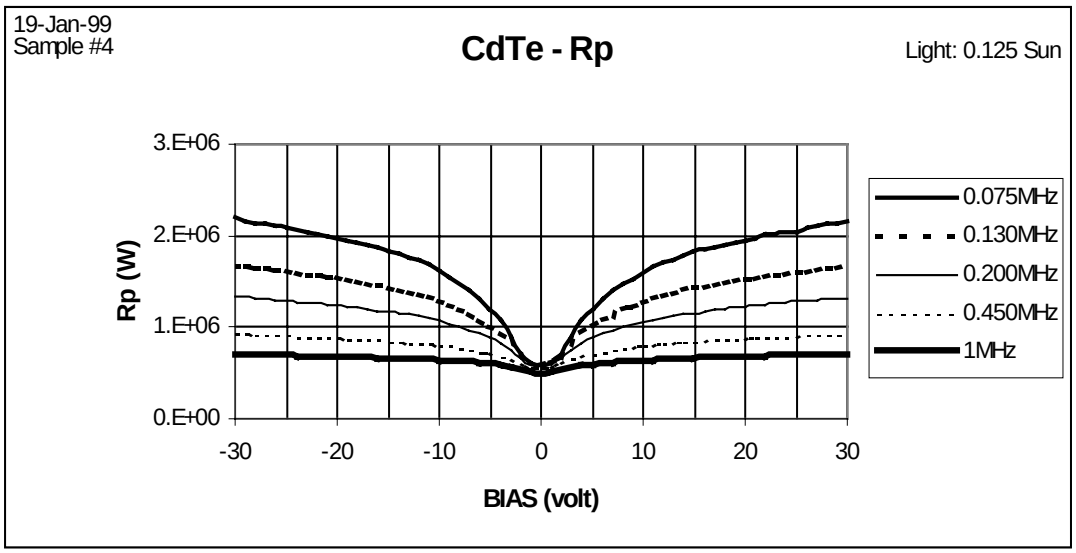

Figure 2.6 Influence of bias applied to the gold electrodes on the CdTe thin film resistance. Illumination intensity is 0.125 Sun. Resistance was measured in "p-mode".

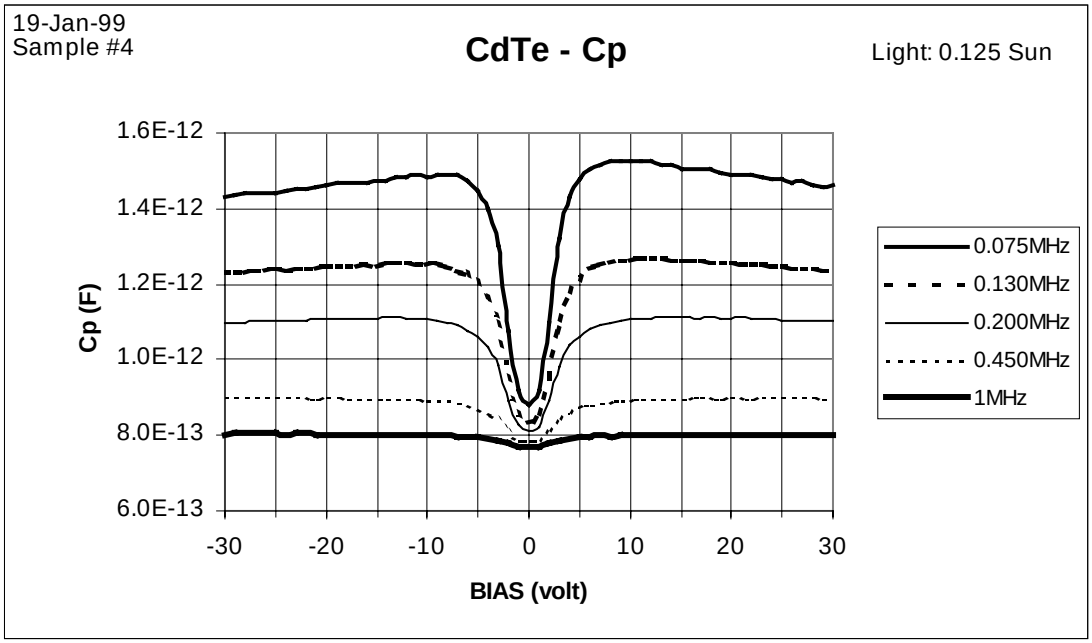

Figure 2.7 Influence of bias on the CdTe thin film capacitance measured in "p-mode". Light intensity is 0.125 Sun illuminated from the film side.

Fig. 2.8a illustrates the situation for zero bias voltage when current is absent and the whole system is in an equilibrium state. Deep GB states donate their electrons to the acceptor levels in the bulk material (trap holes), thus acquiring a positive electrical charge. This leads to the appearance of a potential barrier for the positively charged carriers (holes). Occupation of the GB states (traps) by holes increases until the Fermi level position in the GB region equals its position in the grain bulk. Band bending leads to the depletion layer appearance in the bulk material adjacent to the GB. The total negative space charge in the depletion layers on both sides of the GB is equal to the sheet positive charge of the GB. The width of the GB region W_{GB} has been drawn to be of comparable size to the depletion layer widths, W_l and W_r, for ease of illustrating. For real materials of interest, $W_{GB} << W_l, W_r$.

Fig. 2.8b illustrates changes in the energy band diagram and GB states occupation with holes for the applied bias voltage ("+" at the left grain and "-" at the right one). When equilibrium is disturbed, current flows through the GB from left to right, and Fermi level positions at the left and right grains and in the GB region (E_F^l, E_F^r, and E_F^{GB}) are different. Under new conditions the rate of hole capturing by the GB states and the rate of their emission back to the valence band both are changed. A new dynamic equilibrium state corresponds to higher occupancy of the GB states by holes, that is to higher positive charge of the GB. Based on this physical model, the J-V characteristics were modeled in [27] for different possible distributions of the GB states densities over the bandgap. It could be seen that the excess hole accumulation by the GB leads to increase in resistance.

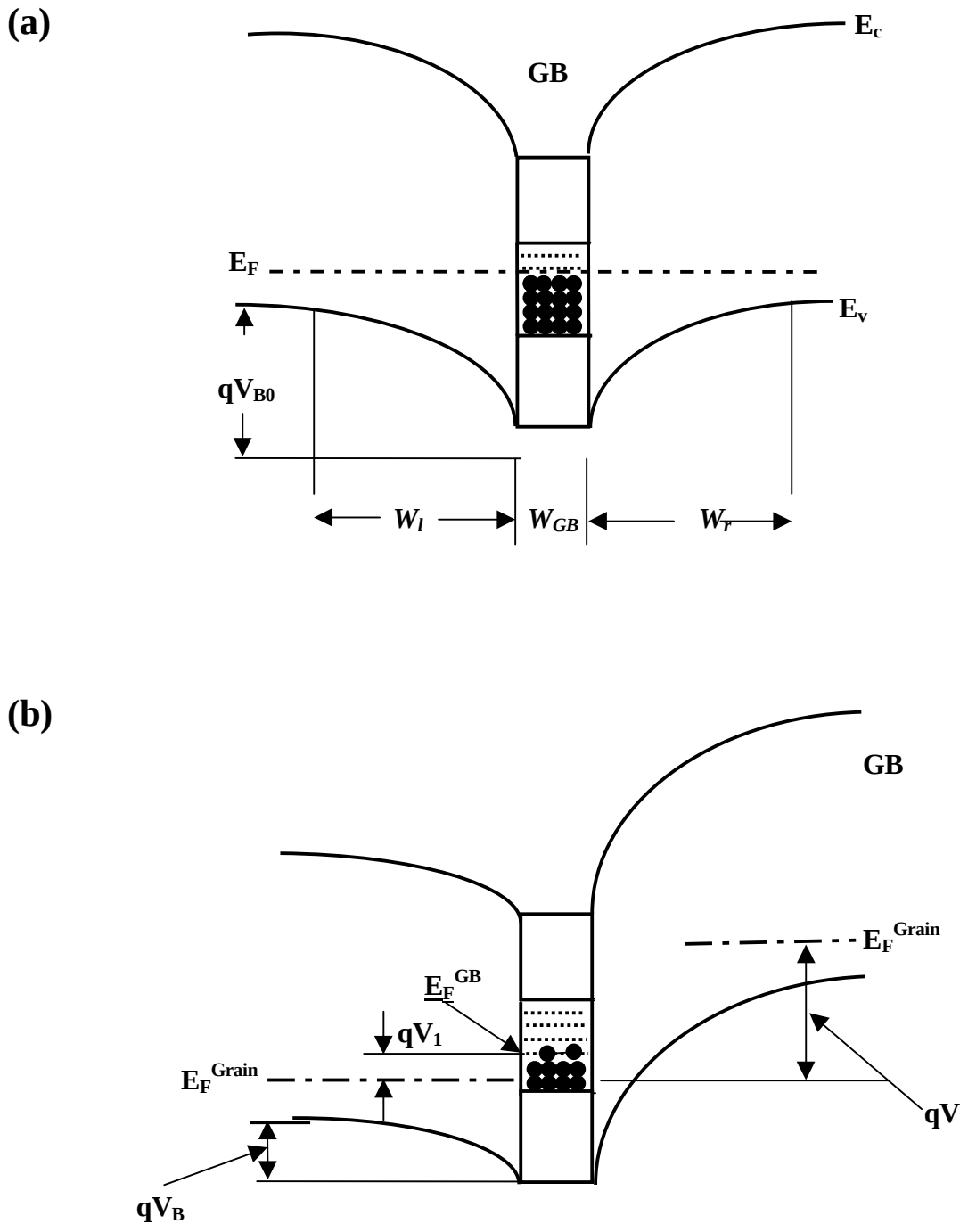

Figure 2.8 Energy-band diagram for two grains of p-type material and their boundary region. Majority carriers (holes) are trapped by the GB states creating a positively charged plane and potential barrier for holes. (a)Band bending in the grains and filling of the GB states by electrons at zero applied bias votage. (b) The same for the non-zero bias; density of trapped holes increased.

The strength of this effect and the dependence on bias voltage is influenced by GB states density and its distribution over an energy range, as well as by the doping level in the bulk

material. The results of the model were compared in this paper with experimental data on Si and Ge bicrystals and on polycrystalline ZnO varistors. The same approach was used in [28] for analysis of current-voltage nonlinearities and influence of light in the p- and n-type CdTe bicrystals. The GB parameters evaluated included the conductivity activation energy, the GB diffusion potential, the energy distribution of the GB states, the minority-carrier recombination velocity, the majority-carrier capture coefficient, and the optical cross section of the GB states.

Thus studies of J-V dependencies of polycrystalline material in a wide bias voltage range can provide valuable information on the electronic GB properties. We are planning to use a similar approach and models in our studies of polycrystalline films. However, it should be mentioned that the bias voltage applied to the single boundary in the experiments presented in [27] ranged up to 100 V, and in [28] up to 24 V. In our films the average grain size is on the order of 10^{-4}cm, therefore the number of grain boundaries between electrodes is on the order of 10^2-10^3. The total bias voltage is divided between numerous GB, hence the voltage per single GB is rather small. In our experiments it did not exceed 0.3-0.5 V. Fortunately, in AC measurements one obtains bias dependence of dynamic resistance, R=dV/dJ. The derivative data emphasizes all non-linearities and makes more visible specific features of J-V characteristics. Our preliminary experiments presented above indicated a significant variation of R even in a relatively narrow bias voltage range.

These experiments demonstrated also a considerable and quite measurable $C(V_{bias})$ dependence. In the rest of this section we will focus on this effect. Our preliminary experiments and modeling showed that $C(V_{bias})$ measurements, even at moderate bias voltage, may become a good method for studies of GB electronic states and their transformation under different processing procedures.

2.4 Capacitance Dependence on Bias Voltage

2.4.1 Two Mechanisms of the GB Capacitance

Capacitance of the GB region includes at least two components of different nature and different dependence on bias voltage. Both were discussed in [29, 30]. The first component is due to the presence of depleted (semi-insulating) layers on both sides of the GB. The specific capacitance, C_1^{sp} (per unit area for a single GB) is described by the equation:

$$C_1^{sp}=\varepsilon\varepsilon_0/(W_l + W_r) \qquad (2.3)$$

At zero bias voltage $W_l=W_r=W$, and

$$C_{10}^{sp}=\varepsilon\varepsilon_0/2W \qquad (2.4)$$

When bias is applied, C_1^{sp} is a series combination of the capacitance of the forward and reverse-biased space charge regions. Since the built-in potential in the forward-biased side, falls only slowly ($V_B \approx V_{B0}$), its capacitance is nearly constant and is approximately $2C_{10}^{sp}$. The capacitance of the reverse-biased side decreases with the applied bias voltage, V. According to [31], the total measured "geometry" capacitance, $C_1(V)$, can be successfully described by equation:

$$\{[2C_{10}/C_1(V)]-1\}^2=1+(V/V_{B0}) \qquad (2.5)$$

Thus the theory predicts a decrease in C_1 as the bias voltage increases, while our measurements showed that at moderately high frequencies the measured capacitance can increase. A similar effect was observed and discussed for silicon bicrystals [29] and ZnO varistors [30]. It was attributed to another capacitance component (different mechanism of AC carrier transport through the GB region).

The key to understanding this mechanism is to realize that the amount of charge trapped at the GB depends on the applied voltage. The voltage applied across the GB in measurements has a DC and a small AC component:

$$V(t)=V_{Bias}+V_{AC}\sin\omega t$$

V_{Bias} determines the steady state charge trapped by the GB states, hence the barrier height, and the real and imaginary parts of the impedance/admittance corresponding to the hole grain-to-grain transport (AC current, J_{G-G}). The equivalent circuit is presented in Fig. 2.2 where intragrain resistance could be neglected. The imaginary part of this admittance is defined by frequency and the "geometry" capacitance, C_1.

At the same time, the AC voltage leads to small oscillations of the trapped charge and hence causes additional component of the AC current (carrier transfer between grain and GB states), J_{G-GB}. The phase of this current is shifted by 90^0 with respect to the AC voltage phase. Indeed, in the beginning of a positive half-period of voltage oscillation, the amount of holes trapped increases (current is positive) until AC voltage achieves its maximum. With the subsequent decrease in voltage, detrapping takes place, and current flows in the opposite direction until in the second half-period the voltage comes to its minimum. After this point the current direction changes again. Thus the GB trapping-detrapping mechanism can be treated in terms of an additional capacitor, C_2, connected in parallel with the geometry capacitor, C_1. A similar explanation of the mechanism was proposed in [29,30], in a slightly different manner. It will be shown below that $C_2=0$ at zero bias and increases as bias voltage increases over some limited range.

The portion of the hole current captured by the GB states, that is ratio J_{G-GB}/J_{G-G}, depends on the density of GB states, in the vicinity of the Fermi level in the GB region, $N_{GB}(E_F^{GB})$, see Fig. 2.8. Our further analysis will be mostly aimed at defining the relationship between this parameter and C_2. J_{G-GB}/J_{G-G} value also depends on the cross-section for hole capturing, transport mechanism, etc. The influence of all these issues can be phenomenologically described by introducing some resistor connected in series with C_2. Thus the whole equivalent circuit we will use for the analysis of our AC measurements will be as shown in Fig. 2.9.

When fitting our AC measurements of CdTe films with this electrical model, it was found that R_3 is orders of magnitude smaller than R_1 and R_2. Its variation in reasonable limits does not influence the fitting value of capacitance, at least in the frequency range of f<5MHz. If we neglect R_3, the capacitance value measured in "p"mode is described by equation:

$$C_p=C_1+C_2/[1+(R_2C_2\omega)^2] \qquad (2.6)$$

It is seen that for the given R_2 and C_2 values, the contribution of the second component to the total measured capacitance decreases as the frequency increases, which allows us to separate C_1 and C_2. This result is in agreement with our experimental data (Fig. 2.7) and also consistent with observations and discussion in [29, 30]. The contribution of C_2 also decreases with increase

in R_2. It was found that illumination of the sample diminishes R_2 which makes the capacitance dependence on bias voltage more pronounced and easier to measure.

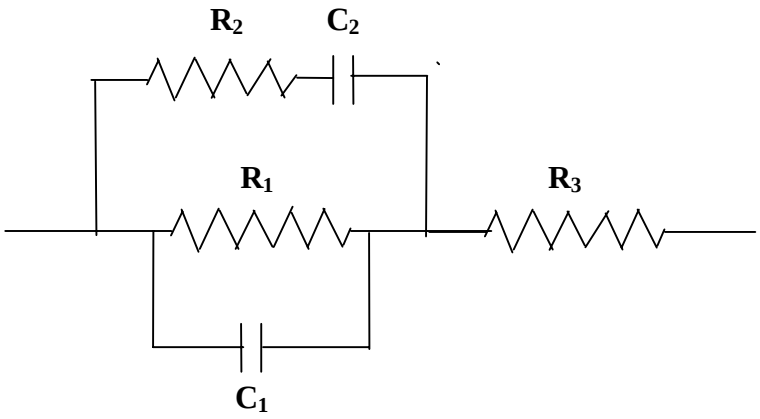

Figure 2.9 Equivalent electrical circuit for the polycrystalline film. R_1 and C_1 are related to the grain-to-grain electrical transport, R_2 and C_2 to the grain-to-grain boundary transport, and R_3 represents resistance of the intragrain material.

2.4.2 Capacitance Caused by the Oscillating GB Electrical Charge

In our analysis of the $C_2(V)$ dependence we used the same approach and basic equations as in Ref. 27. In particular, it was assumed that thermionic emission is the dominating carrier transport mechanism over the GB potential barrier, and the abrupt depletion layer was used. But we have also made two assumptions that simplified the problem:

(a) The bias voltage applied is small, $V \leq V_{B0}/2$ (see Fig.2.8).

(b) The GB density of states is constant: $N_T(E)=\text{const.}=N_T$. Here N_T is the area density of the GB states per unit interval of energy.

The reason for the first assumption is that in our measurements we are not able to apply a high bias voltage to a single boundary because there are a great number of grains between the electrodes. The second assumption arises from the first one. Indeed, a small-applied bias voltage leads to a small change in occupation of the GB states band with majority carriers, hence to a small shift in E_F^{GB} relative to this band. Within this small shift the GB density of states should not vary significantly. These two assumptions enabled us to obtain simple analytical expressions and equations for effects and quantities of interest. That simplified our analysis and our understanding of the physical nature of some observed experimental features. The final equations that will be used for analysis of the data are discussed below.

The dependence of the "GB oscillating charge" capacitance on voltage applied to a single GB, V, is described by the equation:

$$C_2=\{2C_{10}/[1+8C_{10}^{sp}/q^2N_T]\}\times \tanh(qV/2kT), \qquad (2.7)$$

This dependence tends to saturation when qV value achieves and then exceeds 2kT, which is 0.0516 eV at T=300^{0}K. Thus

$$C_2(V_{bias})/C_{10}= (C_2^{sat}/C_{10})\tanh(x), \quad (2.8)$$

where

$$x=(q/2kT)V=(q/2kT)V_{bias}/N_{GB} \quad (2.9)$$

and the number of the GB between electrodes, N_{GB}, is

$$N_{GB}=l/d \quad (2.10)$$

with *l* being the distance between electrodes and *d* an average size of the grains.

Fig. 2.10 shows the experimental data for one of the CdTe thin films prepared with PVD method at IEC. The film thickness is 2.3 μm and the distance between gold electrodes is 1.8 mm. To decrease the sample resistance it was illuminated with white light with 0.125 standard light intensity.

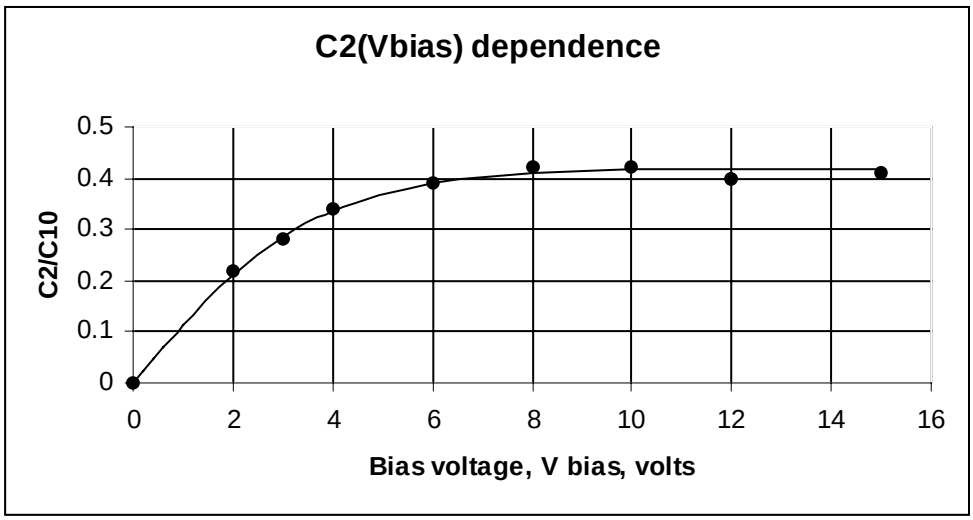

Figure 2.10 Dependence of the "GB oscillating charge" capacitance on bias voltage applied to the sample of PVD CdTe thin film. Points represent the experimental data; solid line represents calculations according Eqs. 2.8 and 2.9 with fitting parameters C_2^{sat}/C_{10}=0.41and N_{GB}=140

The fitting of experimental data can be considered as quite satisfactory. An average grain size, *d*, estimated from the fitting parameter N_{GB} by using Eq.2.10 is of about 1.3 μm, in agreement with the estimate based on AFM images. An estimated maximum bias voltage per single GB is $V^{max} = V_{bias}^{max}/N_{GB} \approx 0.11$V. That satisfied the condition of small bias voltage ($V \le V_{B0}/2$) which we used when deriving the equations for C_2.

The density of the GB states, N_T, can be determined from the experimental data as

$$N_T=(8/q^2)\times\alpha/(2-\alpha)\times C_{10}^{sp}, \quad (2.11)$$

where $\alpha=C_2^{sat}/C_{10}$, or as

$$N_T,\ cm^{-2}(eV)^{-1}=5\times10^{19}\times\alpha/(2-\alpha)\times C_{10}^{sp},\ F\times cm^{-2} \quad (2.12)$$

For the sample under discussion, the measured value of C_{10} is of 0.95 pF. Based on the film thickness (2.3 μm), number of grains between electrodes (140) and the film width (10mm), one may evaluate the value of a specific capacitance: $C_{10}^{sp} \approx 6\times10^{-7}$F. As shown above, $\alpha= C_2^{sat}/C_{10}=0.41$. **Thus, the estimated density of GB states, N_T, is about 7×10^{12} $cm^{-2}eV^{-1}$**. Since the bias applied is small, this value is approximately equal to the GB density of states at the GB Fermi level for the unbiased GB. The obtained value of N_T is rather high but it is within a reasonable range (see [28]). Similar measurements were made on other PVD CdTe films with different treatments. Estimates of N_T varied in the range of 10^{12} to 10^{13} $cm^{-2}eV^{-1}$. This was in the same range as the estimate for CdTe films lifted from the CdS layer in the CdS/CdTe/TCO structure prepared by CSS at NREL. These samples were provided by L. Woods.

At this time no systematic comparable studies were performed on the different processed films. These studies are to be performed in Phase II of this project. We plan to continue and complete analysis of the bias dependence of the dynamic resistance. Combined studies of C(V) and R(V) dependencies should provide more reliable information on electronic properties of the GB. We will also study these dependencies in a temperature range and under illumination with controlled light intensities. That can provide information on the barrier height, GB states position in the energy spectrum, cross-section of carrier capturing by the GB states, kinetics and mechanisms of their recharging, etc. The influence of S and Cu diffusion into CdTe films on GB properties will also be studied.

2.5 Major Results and Conclusions

1. Various measurement modes provided by a recently acquired LCR meter were made for measuring impedance of thin films as a function of frequency and bias voltage. Modeling of the measured dependencies was performed using various physical and electrical models. By fitting the measured and calculated frequency dependencies one can determine individual contributions of the GB and IG material to the measured sample resistance as well as the GB capacitance. Then, based on the sample geometry and average grain size, one can estimate specific GB resistance and capacitance per single GB of unit area, as well as the IG material resistivity.
2. Contribution of the IG material to the total measured resistance of the CdTe and CdS thin polycrystalline films is 10^3-10^6 times lower than that of the GB, so that the resistance is totally defined by the GB. The GB potential barrier height, Φ_B, values estimated based on the thermionic emission theory are on the order of several tenths of electron-volt, in agreement with the estimates in Ref. 26.
3. The high photoconductive effect in polycrystalline CdTe and CdS thin films is totally due to decrease in the GB resistance. The latter depends exponentially on Φ_B, therefore even a small change in Φ_B caused by light can lead to a dramatic change in R_{GB}.

4. Based on specific GB capacitance value in the CdTe films, the doping level in the GB region was estimated to be in the range of 10^{17} to 10^{18} cm^{-3}. These values are orders of magnitude higher than the average doping level in the CdTe layer of a cell determined from C-V profile. Our estimates are in good agreement with those made in [26] based on temperature dependence of electrical resistance. It follows from the measured IG resistance that thickness of highly doped layer adjacent to the GB is on the order of tens of nm.
5. A considerable increase was observed in film resistance and capacitance caused by application of bias. Increase in resistance was attributed to increase in the GB electrical charge and potential barrier due to bias. The increase in capacitance was attributed to the additional component of the GB capacitance, C_2, provided by oscillating of the GB electrical charge under oscillating voltage.
6. The equation was derived that describes dependence of C_2 on bias voltage,V, applied to a single GB: $C_2(V)=C_2^{sat}\tanh(qV/2kT)$. The $C_2(0)$ and $C_2(V)$ dependence saturates in a bias range ~0.1 V (at room temperature). The results of theory fit very well the experimental data and provide an additional independent option to evaluate average grain size. From the ratio $C_2^{sat}/C(0)$, one can estimate the density of the GB electronic states, N_T. For the films we have investigated, the N_T value is in a range of 10^{12} to 10^{13} $(cm^2\ eV)^{-1}$

The most important conclusion from the studies presented in this section is that AC measurements with LCR meter is an effective method for investigation of electronic properties of thin polycrystalline films like CdTe and CdS thin films. We have not yet used and even understood all the options provided by this method and will develop this methodology further. New experiments should reveal specific features of measured parameters and their dependencies on bias, illumination, temperature, etc., for the films prepared with varying processing procedures. Proper analysis of electrical properties together with film composition, structure, type and content of a dopant should provide a better understanding of the basic electronic properties and their dependence on processing.

3. Study of Cell Degradation under Stress Conditions

3.1 Technical Approach and Objectives

This section presents some results of our studies of the degradation under stress conditions of the CdS/CdTe solar cells with a ZnTe:Cu/Au back contact. Our previous studies of degradation were mostly performed under the following stress conditions: enhanced temperature, vacuum, dark, open circuit. Only few, non-systematic studies of degradation were made with a bias applied to a cell. Initial results and their analysis indicated that electromigration of mobile defects and impurities, especially of the Cu dopant, should be taken into account when analyzing the degradation mechanisms. The major goal of the studies we started in Phase I of the project was to find and analyze manifestations of electromigration of the electrically charged defects and impurities that are responsible for the degradation of a cell. To make this possible we conducted the stress tests in dark and light under different external biases.

One must keep in mind that even at the absence of an external bias, a strong built-in electric fields exist in a cell, that may cause electromigration of defects and influence its rate. The built-in potentials and the electric fields are different in dark and light. It is clear also that external biases applied to the cell change the magnitude and distribution of the electric fields over the cell thickness, hence providing changes in electromigration processes.

If we do not consider the electric fields in the GB regions due to the GB electrical charge, there are two regions in the cell with high electric fields (one-dimension model). The first one is the depletion layer adjacent to the CdTe/CdS junction. Under the open circuit condition (V_{bias}=0) in dark, the width of this layer is about 1.5 μm and the average electric field is of the order of 10^4 V/cm. Illumination of a cell with 1 Sun intensity decreases the built-in potential by an amount of about 0.8 V. The depletion layer shrinks considerably and the electric field diminishes significantly. The second region with a considerable electric field is the CdTe layer adjacent to the back contact interface. There are many indications that a Schottky diode usually exists at this interface with a potential barrier for the majority carriers (holes in our case). In the as-prepared cell this barrier is low and thin enough to provide tunneling through the barrier and sufficiently low "series resistance". But aging of a cell, especially under stress conditions, leads to the development of a stronger barrier which manifests itself in an increase of “series resistance”. Initially there already exists a built-in potential and electric field that can influence the migration of charged defects in this region. This effect should become more important in the aged or stressed cells. We also have found that the resistance of the back contact Schottky diode decreases significantly in light. That could be due to a change in transport mechanism. However, it should not be excluded that positive electric charge accumulated in the interface states might diminish in light. If so, the Schottky barrier height, depletion layer width and electric field should decrease, and changes in electromigration may take place.

The major objectives of the studies in Phase I were:

- Studying degradation of the cells under widely varied stress conditions to clarify what conditions provide the most severe degradation of a particular cell parameter
- Searching for reversible effects under consecutively changed applied biases

- Application of different methods and techniques for the degraded cell characterization to choose the most informative ones.
- Planning new degradation studies in Phase II based on results and conclusions of Phase I.

3.2 Experimental Results and Discussion

Cells were fabricated using the Glass/TCO/CdS/CdTe structures supplied by Solar Cells, Inc. (now First Solar). The back contact was applied in our facilities. Multilayer structure consisting of the Cu, ZnTe, and Au layers was consequently deposited on the preliminary etched, rinsed and dried CdTe surface. The consecutive deposition of the Cu and ZnTe layers instead of coevaporation previously used provided more precise control of the Cu amount. No considerable difference in the initial performance of a cell was found for these two methods of the back contact preparation. No difference was found in the degradation rate for the same stress conditions such as enhanced temperature, vacuum, dark, open circuit.

All the stress tests were performed on un-encapsulated cells in air. To activate the degradation processes, stress conditions included an elevated temperature of 100^0C. When stressing in light, about 1 Sun intensity was used. In the course of degradation the J-V (light and dark) and C-V (dark) dependencies were periodically measured. Some results of stress testing are presented in Table 3.1. It can be seen from the table that stresses under different applied biases lead to different changes in the cell parameters. It is also seen that the results of stressing under the given bias conditions can differ considerably for stressing in dark and light.

The highest degree of degradation of all parameters was observed for the negative bias in dark. The "series resistance" defined as dV/dJ at $V=V_{oc}$ for the J-V dependence measured in light, increased more than 25 times. Lower, but also significant, increase in R_{se} took place under O.C. condition. In light R_{se} degrades much less, especially under S.C. and V_{mp} conditions. R_{sh} also degrades strongly in dark and much less in light. Moreover, for {L, S.C. and L,V_{mp}} R_{sh} increases after stressing. V_{oc} degrades considerably at negative bias both in dark in light, but in dark the change is greater. The lowest degradation of V_{oc} takes place at {L, S.C. and V_{mp}} conditions. Contrary to V_{oc}, the short circuit current, J_{sc}, even increases at {L, O.C. and Fwd} while it degrades significantly at {L, S.C. and V_{mp}} for 113 h testing. Again, the most severe degradation is seen for {D, Neg.} conditions.

Table 3.1. Changes in the cell parameters as a function of stress test conditions and length (time). Data are averaged over a number of cells stressed under the same conditions. Designations for the stress conditions: D - dark, L - light, Neg.- bias V≈-1V, S.C. - short circuit (V=0), V_{mp} - bias corresponds to the maximum power, O.C. - open circuit (J=0), Fwd - J= +5 mA/cm^2.

Stress time, h	Stress conditions						
	D, Neg	D, O.C.	L, Neg	L, S.C.	L, V_{mp}	L,O.C.	L, Fwd
				Δ Eff., %			
24	-50	-24	-22	-6.5	-9	-21	-20
113	-60	-44	-24	-21	-13	-6.7	-19
				Δ Voc, %			
24	-12	-2.3	-6.4	-4.3	+0.9	-0.5	-4.8
113	-8.7	-4.6	-7.0	-5.5	-1.4	-0.8	-7.0
				Δ Jsc, %			
24	-15.5	0.0	+1.1	+2.2	-3.0	+1.6	+2.9
113	-13.5	-4.3	-0.9	-9.9	-4.7	+1.1	+7.7
				Δ Rse, %			
24	+2500	+440	+145	+22	+40	+230	+140
113	+2500	+820	+250	+75	+35	+80	+120
				Δ Rsh, %			
24	-70	-48	-21	+43	+20	-26	-18
113	-70	-65	-10	+45	+23	+2.8	-30.3

In order to achieve better understanding of the degradation mechanism, particularly the role of electromigration, we conducted some stress tests consecutively applying different biases to the same cells. Stress testing was conducted in dark at the temperature of 100^0C. Cells were characterized before stressing, after stress test under bias for 20 h, and then after additional stressing for 20 h under another bias. Some results of these studies are presented in Table 3.2.

Table 3.2 Stress tests under varied bias

Stress conditions	Eff.,%	J_{sc}, mA/cm^2	V_{oc}, mV	R_{se}, Ω-cm^2	R_{sh}, Ω-cm^2
Before Stress	11.5	21	825	2.7	560
O.C., 20 h	8.7	20	770	16.7	305
O.C., +20 h	7.7	18.8	760	20.8	290
Before stress	11.4	20.5	805	2.7	725
Fwd., 20 h	11.4	20.0	825	2.0	730
Fwd., +20 h	10.2	19.5	810	2.7	600
Before stress	11.3	20.8	805	3.5	695
Neg., 20 h	7.7	20.2	745	86	680
Neg., +20 h	7.2	20.1	735	86	540
Before stress	10.6	20.5	780	1.8	470
Fwd., 20 h	10.8	19.8	800	2.1	570
O.C., +20 h	9.1	19.8	755	4.8	370
Before stress	10.5	20.0	785	1.9	544
Fwd., 20 h	10.0	19.3	780	1.9	540
Neg., +20 h	7.4	18.8	730	25.5	440
Before stress	10.9	21.0	780	2.8	620
Neg., 20 h	7.6	20.5	740	45.5	660
O.C., +20 h	6.2	17.2	740	22.5	315
Before stress	10.4	19.7	785	3.0	650
Neg., 20 h	6.9	19.3	735	60	640
Fwd., +20 h	6.9	20.0	685	6.9	550

The results should be considered only as preliminary, however some of them seem to be indicative and deserve to be mentioned:

- The highest degree of the R_{se} degradation for 20 h testing is observed for the Neg. stress, the lowest (zero or even R_{se} improvement) for Fwd. stress, and O.C. provides some intermediate increase in R_{se}. O.C. stress after Fwd. leads to some increase in R_{se}, O.C. after Neg. decreases R_{se}. Fwd. after Neg. provides a considerable recovery of R_{se}. Neg. after Fwd. causes a significant increase in R_{se}, but its final value is three times lower than for Neg. stress only.

- Fwd. and Neg. stresses for 20 h do not provide any degradation of R_{sh}, while the O.C. stress for 20 h decreases R_{sh} by ~45%. It is seen that additional O.C. stress after Fwd. or Neg. leads to a considerable R_{sh} degradation., while Fwd. after Neg. and vice versa change R_{sh} much less.

- Fwd. stressing itself does not cause a considerable degradation of Voc, but when applied after Neg., it leads to a considerable additional decrease in V_{oc}, which already has degraded significantly due to the Neg. stress. O.C. stress causes 6.5% decrease in V_{oc} if applied after Fwd., but does not change V_{oc} after Neg. This seems to be an observation that is difficult to explain with only electromigration.

The results in Tables 3.1 and 3.2 were used for planning new stress test experiments for Phase II studies of degradation.

3.3 Characterization Methods and Techniques

We measure routinely J-V characteristics of a cell in dark and light after each stress test. These measurements provided the results presented in Tables 3.1 and 3.2. In addition, we computed dV/dJ (dynamic resistance, R) as a function of an applied bias voltage and current through the cell. Our previous analysis [32] performed in the two-diode model showed that based on these dependencies one may evaluate the diode quality factors and saturation currents for both, main diode and back contact Schottky diode, as well as their changes due to stressing. We also use to measure C-V profiles at frequency of 100 KHz to estimate changes in doping levels in the CdTe layer. Unfortunately, analysis of C-V profile is impeded by presence of high "series resistance" in the degraded cells and its dependence on bias, as well as by the capacitance of the back contact Schottky diode.

Our new HP LCR meter provides more options for obtaining information on the electrical properties of the cells, in particular, characteristics of the two diodes. First, the dynamic resistance can be measured directly instead of computation of the dV/dJ derivative of a static J-V characteristic. This resistance can be measured as a function of frequency as well as applied bias. Based on our experience with measurements of impedance in different modes and its modeling for complicated equivalent electrical circuits (see Sec.2), we are able, in principle, to separate and study independently dynamic resistance and capacitance of the two diodes. We are also able to study frequency and bias dependencies of these parameters in dark and light. Our preliminary cell measurements with using LCR meter seem promising. Hopefully, in the Phase II degradation studies we will be able to obtain in this way more detailed and reliable data on changes in the cell properties after stress testing.

3.4 Major Results and Conclusions.

- Stress tests of the cells under various stress conditions revealed conditions providing the most severe degrading of different cell parameters
- Consecutive stress testing under different bias revealed some reversible effects
- Preliminary analysis of the data obtained demonstrated a significant role of electromigration of the charged defects/impurities
- Some new approaches for the cell characterization and the data analysis were developed and checked experimentally
- New stress test experiments were planned for continued studies of degradation mechanisms

4. Team Activities

4.1 Studies of the High Resistance Tin Oxide Films (HRT)

We have characterized three samples undoped HRT/Glass that were deposited at different temperatures by ITN. The measured film thicknesses were in a range 500 to 700 nm. Measurements of thermopower provided carrier concentration values from $7x10^{19}$ to $9x10^{19}$ cm^{-3}. Transparency averaged over a wavelength range 500 to 800 nm was above 80%. Well manifested diffraction patterns indicated good uniformity of thickness. Mapping of sheet resistance showed also good uniformity of this parameter for two films deposited at higher temperatures. However sheet resistance measured on the low-temperature film was non-uniform. For the Hall effect measurements, small samples were cut. The two samples with higher deposition temperature had Hall carrier concentration values close to those obtained with thermopower measurements. The low-temperature sample Hall concentration was an order of magnitude lower, perhaps caused by high non-uniformity of sheet resistance. The Hall mobility values were in a range from 2 to 6 cm^2/Vs .

4.2 Cell Stability Tests at the First Solar Facilities

We have prepared and characterize the cells with the ZnTe:Cu/Au back contact on the CdTe/CdS/TCO substrates supplied by First Solar, LCC. After completion, these cells were sent in February 1999 to the First Solar for comparative stress testing at its facilities under various stress conditions. The goal of these tests in which various institutions participate is to compare stability/degradation rate of the cells produced with different back contact structures and processing.

4.3 Characterization of Materials Received from First Solar

As part of the First Solar Focus Group we have characterized partially completed structures that showed variability in cell degradation in initial studies. The measurements included spectroscopic ellipsometry, atomic force microscopy and x-ray diffraction.

5. References

1. C. G. Granqvist, *Appl. Phys., A*, **19,** 57 (1993).
2. G. Haacke, *J. Appl. Phys.* **47,** 4086 (1976).
3. B. D. Cullity, Elements of X-Ray Diffraction, Addison-Wesley, Reading, MA,1978
4. N. Cusack and P. Kendall, *Proc. Phys. Soc.* **72**, 898 (1958).
5. R. B. Roberts*, Philos. Mag,* **36,** 91 (1977).
6. M. J. Laubitz, T. Matsumura, and P. J. Kelly, *Can. J. Phys.* **54,** 92, (1976).
7. H. M. Ahmad and D. Greig, *J. Phys. (Paris),* **35,** C4-223 (1974).
8. The Temperature Handbook, Vol. 29, Omega Engineering, Inc. 1995.
9. W. P. Mulligan, "A study of the Fundamental Limits to Electron Mobility in Cadmium Stannate Thin Films", Ph.D. thesis. Dept. of Material Science. Colorado School of Mines.
10. Y. Qu,"A Study of Transparent Zinc Oxide Thin Films", Ph.D. thesis. Dept. of Physics. Colorado School of Mines.
11. A Short course in Ellipsometry, © J. A. Woollam Co., Inc.
12. O. J. Heavens, Optical Properties of Thin Solid Films, Dover Publications, Inc., New York, 1991
13. C. Wolden, Private Communication
14. Selected Powder Diffraction Data for Metal and Alloys, International Centre for Diffraction Data, Pennsylvania, 1978.
15. V. I. Kaydanov, Thin Film Thermoelements: Physics and Applications, "Nauka", Moscow,1985.
16. B. M. Askerov, Electron Transport Phenomena in Semiconductors, World Scientific, Singapore, 1994.
17. O. Madelung, Semiconductors other than Group IV Elements and III-V Compounds, Springer-Verlag, Berlin-Heidelberg, New York 1992.
18. C. Herring, E. Fogt, *Phys. Rev.* **101,** 944 (1956).
19. E. Shanti, V. Dutta, A. Banerjee, and K. L. Chopra, *J. Appl. Phys.* **51** 6243 (1980).
20. G. Sanon, R. Rup and A. Mansingh, *Phys. Stat. Sol.(a)* **135,** 581 (1993).
21. E. M. Conwell, V. F. Weisskoft, *Phys. Rev.* **77,** 388 (1950).
22. H. Brooks, *Phys. Rev. A*, **38**, 879 (1951).
23. H. Brooks, *Advances in Electronics and Electron. Phys***. 7**, 87 (1955).
24. R. Mansfield, *Proc. Phys. Soc. B*, **69,** 79 (1956).

25. J.J. Kester, S. Albright, V. Kaydanov, R. Ribelin, L.M. Woods, J.A. Phillips, *NREL/SNL PV Program Review, Proceedings of the 14th Conference, Lakewood, CO 1996*; AIP Conference Proceedings, pp.162-169

26. L.M. Woods, D.H. Levi, V. Kaydanov, G.Y. Robinson, and R.K. Ahrenkiel, *Proceedings of the2nd World Conf. on Photovoltaic Solar Energy Conversion*, July 6-10, 1998, Vienna, Austria, pp. 1043-1046.

27. G.E. Pike and C.H Seager, *J. Appl. Phys.* **50**(5), 3414 (1979).

28. T.P. Thorpe Jr., A.L. Fahrenbruch, and R.H. Bube, *J. Appl. Phys.* **60**(10), 3622 (1986).

29. C.H. Seager and G.E. Pike, *Appl. Phys. Lett.* **37**(8), 747 (1980)

30. G.E. Pike, Grain Boundaries in Semiconductors, Elsevier Science Publ. Co., Inc., 1982, p.369

31. M.G. Spencer, W.J. Schaff and D.K. Wagner, *J. Appl. Phys.* **54**(3), 1429 (1983)

32. D. Morgan, J. Tang, V. Kaydanov, T.R. Ohno, and J.U. Trefny, *NCPV Photovoltaic Program Review, Proc. of the 15th Conf.*, Denver, CO, 1998, pp.200-205.

6. Acknowledgements

Many individuals, in addition to those at the Colorado School of Mines, have contributed to this work over the past year. Brian McCandless of the Institute of Energy Conversion prepared PVD CdTe thin films for our AC measurements. Collaboration and discussions with Larry Woods (NREL) were very helpful for us when starting these studies. We are thankful to Rick Powell and Doug Rose of First Solar, LCC., for supplying us with the materials for CdTe/CdS cells preparation and studies of degradation. It is hard to underestimate the value of discussions of our research approach and results that we have had with the individuals mentioned above and also Tim Coutts, Tim Gessert, Dave Albin, Jim Sites, Peter Meyers, and other scientists involved in fabrication and studies of the CdTe/CdS solar cells. We greatly appreciate the encouraging interest in our activities, discussions and suggestions we get constantly from Kenneth Zweibel, Harin Ullal, and especially from our contract monitor, Bolko von Roedern.

7. Appendices

7.1 Personnel

Many individuals contributed to this work. Their names, titles, and representative responsibilities are summarized below.

Timothy R. Ohno, Associate Professor of Physics: Photovoltaic Development, Surface Physics, Principal Investigator

Victor I. Kaydanov, Research Professor of Physics: Photovoltaic Development, Electron Transport Phenomena, Principal Investigator

Reuben T. Collins, Professor of Physics: Electronic and Optical Properties of Semiconductors

Don L. Williamson, Professor of Physics: Structural Properties of Materials, XRD

Thomas E. Furtak, Professor of Physics: Optical Properties of Semiconductors, Ellipsometry

Uri Laor, Visiting Scientist: Impedance Spectroscopy of Thin Polycrystalline Films

Aklesh Gupta, Post. Doc.: CdTe Cell Processing and Characterization

Tinjung Wen, Research Associate: TCO Processing and Characterization

Collin Wolden, Assistant Professor of Chemical Engineering: APCVD System Design

Wenjie Song, Graduate Research Assistant: CdTe Electrodeposition and Cell Optimization. (defended PhD thesis January 1999)

Don Morgan, Graduate Research Assistant: Degradation of Solar Cells

Ahmed Alkaoud, Graduate Student: Tin Oxide Processing and Studies (defended PhD thesis March 1999)

Angelo Gilmore, Graduate Research Assistant: Ellipsometry of Multilayer Structures, TCO

Scott Townsend, Graduate Research Assistant: ZnTe Back Contact, Cell Stability

M. Hasan Aslan, Graduate Student: Photoluminescence, Interdiffusion Studies
(defended PhD thesis January 1999)

Ahmed Balcioglu, Graduate Student: Surface Analysis and Deep Level Transient Spectroscopy

Brian Egaas, Graduate Research Assistant: Thin Film Solar Cell Fabrication

Wendi Batchelor, Graduate Research Assistant: Thin Film Solar Cell Fabrication

Yoxa Mahathongdy, Graduate Research Assistant: CdTe Solar Cell Processing

Jianping Xi (Green Development, LCC): APCVD System Design, TCO Processing

Lianghuan Feng (Green Development, LCC.): TCO Processing and Characterization

7.2 Laboratory Improvements

Significant laboratory improvements occurred during the initial phase of this subcontract that have permitted more thorough materials characterization.

1. A Hewlett-Packard LCR meter, Model 4285 was added for AC measurements of polycrystalline thin films described in Section 2. Computer interfacing with a graphical programming language, HPVee, provides great flexibility in the type of automated measurements and analysis available.

2. A new tunable Ti-sapphire laser from SpectraPhysics is being used for energy dependent near-field scanning microscope studies.

3. A Nanoscope II scanning probe microscope was added, under the DOE University PV Research Equipment Program, award no. AAD-8-18669-04.

4. A gas phase optical monitoring system was chosen from Ocean Optics in support of subcontract ZAK-8-17619-13, Atmospheric Pressure Chemical Vapor Deposition of CdTe for High Efficiency Thin Film PV. The Ocean Optics spectrometer will be used for absorption studies to monitor Cd and Te vapor concentration.

7.3 Publications

1. "Electrical Characterization of CdTE Grain-Boundary Properties from As Processed CdTe/CdS Solar Cells", L.M. Woods, D.H. Levi, V. Kaydanov, G.Y. Robinson, R.K. Ahrenkiel, *Proc. of the 2nd World Conf. on Photovoltaic Solar Energy Conversion*, July 1998, Vienna, Austria, pp. 1043-1046
2. "Influence of $CdCl_2$ Treatment on the Electrical and Optical Properties of CdS Thin Films", W. Song, D. Mao, J.U. Trefny, R.K. Ahrenkiel, D.H. Levy, and S. Johnston, *NCPV Photovoltaics Program Review, Proc of the 15th Conference*, Denver, CO, 1998, pp. 188-194
3. "Effect of Optimization of CdS/CdTe Interdiffusion on CdTe Electrical Properties and CdS/CdTe Cell Performance", W. Song, D. Mao, V. Kaydanov, T. R. Ohno, J.U. Trefny, R.K. Ahrenkiel, D.H. Levi, S. Johnston, B.E. McCandless, Ibid. pp. 194-199
4. "Degradation Mechanism studies in CdS/CdTe Solar Cells with ZnTe:Cu/Au Back Contact", D. Morgan, J. Tang, V. Kaydanov, T.R. Ohno, and J.U. Trefny, Ibid. pp.200-205
5. "Atmospheric Pressure Chemical Vapor Deposition of SnO_2: Processing and Properties", A. Al-Kaoud, T. Wen, A. Gilmore, V.Kaydanov, T.R. Ohno, C. Wolden, L. Feng, J. Xi, Ibid. pp.212-217
6. "Electrical Characterization of Etched Grain-Boundary Properties from As-Processed px-CdTe-Based Solar Cells", L.M. Woods, D.H. Levi, V. Kaydanov, G.Y. Robinson, and R.K Ahrenkiel, Ibid. pp. 499-504
7. "Evidence for Grain Boundary Assisted Diffusion of Sulfur in Polycrystalline CdS/CdTe heterojunctions", M.K. Herndon, A. Gupta, V. Kaydanov and R.T. Collins, submitted to *Appl. Phys. Lett.* , 1999

REPORT DOCUMENTATION PAGE

Form Approved
OMB NO. 0704-0188

1. AGENCY USE ONLY (Leave blank)	2. REPORT DATE	3. REPORT TYPE AND DATES COVERED
	August 2000	Annual Technical Report, Phase I; 15 May 1998–14 May 1999

4. TITLE AND SUBTITLE
Process Development and Basic Studies of Electrochemically Deposited CdTe-Based Solar Cells; Annual Technical Report, Phase I; 15 May 1998–14 May 1999

5. FUNDING NUMBERS
C: XAK-8-17619-28
TA: PV005001

6. AUTHOR(S)
V.I. Kaydanov, T.R. Ohno

7. PERFORMING ORGANIZATION NAME(S) AND ADDRESS(ES)
Colorado School of Mines
Golden, Colorado 80401

8. PERFORMING ORGANIZATION REPORT NUMBER
NREL/ SR-520-28762

9. SPONSORING/MONITORING AGENCY NAME(S) AND ADDRESS(ES)
National Renewable Energy Laboratory
1617 Cole Blvd.
Golden, CO 80401-3393

10. SPONSORING/MONITORING AGENCY REPORT NUMBER

11. SUPPLEMENTARY NOTES
NREL Technical Monitor: B. von Roedern

12a. DISTRIBUTION/AVAILABILITY STATEMENT
National Technical Information Service
U.S. Department of Commerce
5285 Port Royal Road
Springfield, VA 22161

12b. DISTRIBUTION CODE

13. ABSTRACT *(Maximum 200 words)*
The project describes long-term research and development issues related to polycrystalline thin-film solar cells. Our general research approach is based on combining activities aimed at improvement of cell performance and stability with activities aimed at increasing our fundamental understanding of the properties of materials making up the cells: CdTe, CdS, multi-layer back contact, and transparent conducting oxide (TCO) front contact. We emphasize the relation between structural and electronic material properties and various processing procedures, as well as the microscopic mechanisms responsible for the cell performance and its degradation.

Major results and conclusions of this project include:

- Stress tests of the cells under various stress conditions revealed conditions providing the most severe degrading of different cell parameters
- Consecutive stress testing under different bias revealed some reversible effects
- Preliminary analysis of the data obtained demonstrated a significant role of electromigration of the charged defects/impurities
- Some new approaches for the cell characterization and the data analysis were developed and checked experimentally

New stress test experiments were planned for continued studies of degradation mechanisms.

14. SUBJECT TERMS
photovoltaics; CdTe-based solar cells; electrochemically deposited; APCVD SnO_2:F thin films; electrical characterization of CdTe and CdS thin films; cell degradation; Thin Film Partnership Program

15. NUMBER OF PAGES

16. PRICE CODE

17. SECURITY CLASSIFICATION OF REPORT	18. SECURITY CLASSIFICATION OF THIS PAGE	19. SECURITY CLASSIFICATION OF ABSTRACT	20. LIMITATION OF ABSTRACT
Unclassified	Unclassified	Unclassified	UL